[12]Le Floc'h, S., J. Ohayon, P. Tracqui, G. Finet, A. M. Gharib, R. L. Maurice, G. Cloutier, and R. I. Pettigrew. Vulnerable atherosclerotic plaque elasticity reconstruction based on a segmentation-driven optimization procedure using strain measurements: theoretical framework. *IEEE Trans. Med. Imaging* 28:1126–1137, 2009.

[13]Morice, M.-C., P. W. Serruys, J. E. Sousa, J. Fajadet, E. B. Hayashi, M. Perin, A. Colombo, G. Schuler, P. Barragan, G. Guagliumi, F. Molnar, and R. Falotico. A randomized comparison of a sirolimus-eluting stent with a standard stent for coronary revascularization. *N. Engl. J. Med.* 346:1773–1780, 2002.

[14]Nashihara, H., and T. Ishibashi. A possible product design for minute medical parts. Development of self-expanding stent made of memory alloy. *J. Asian Des. Int. Conf.* 1: CD-ROM, 2003.

[15]Nordmann, A. J., M. Briel, and H. C. Bucher. Mortality in randomized controlled trials comparing drug eluting vs. bare metal stents in coronary artery disease: a meta-analysis. *Eur. Heart J.* 27:2784–2814, 2006.

[16]Peterson, L. H., R. E. Jensen, and J. Parnell. Mechanical properties of arteries in vivo. *Circ. Res.* 8:622–639, 1960.

[17]Schweiger, M. J., E. Ansari, G. R. Giugliano, J. Mathew, A. Islam, J. Morrison, and J. R. Cook. Morphology and location of restenosis following bare metal coronary stenting. *J. Invasive Cardiol.* 18:165–168, 2006.

[18]Selzer, R. H., W. J. Mack, P. L. Lee, H. Kwong-Fu, and H. N. Hodis. Improved common carotid elasticity and intima-media thickness measurements from computer analysis of sequential ultrasound frames. *Atherosclerosis* 154:185–193, 2001 .

[19]Srinivas, K., T. Nakayama, M. Ohta, S. Obayashi, and T. Yamaguchi. Studies on design optimization of coronary stents. *J. Med. Devices* 2:11004-1-7, 2008.

[20]Tokita, A., Y. Ishigaki, H. Okimoto, H. Hasegawa, Y. Koiwa, M. Kato, H. Ishihara, Y. Hinokio, H. Katagiri, H. Kanai, and Y. Oka. Carotid arterial elasticity is a sensitive atherosclerosis value reflecting visceral fat accumulation in obese subjects. *Atherosclerosis* 206:168–172, 2009.

[21]Yamagishi, T., M. Kato, Y. Koiwa, K. Omata, H. Hasegawa, and H. Kana.Evaluation of plaque stabilization by fluvastatin with carotid intima-medial elasticity measured by a transcutaneous ultrasonic-based tissue characterization system. *J. Atherosclero. Thromb.* 16:662–673, 2009.

[22]Yazdani, S. K, and J. L. Berry. Development of an in vitro system to assess stent-induced smooth muscle cell proliferation: a feasibility study. *J. Vasc. Interv. Radiol.* 20:101–106, 2009.

[23]Yoshino, D., and K. Inoue. Design method of self-expanding stents suitable for the patient's condition. *Proc. IMechE Part H: J. Eng. Med.* 224:1019–1038, 2010.

[24]Yoshino, D., M. Sato, and K. Inoue. Estimation of force on vascular wall caused by insertion of self-expanding stents. *Proc. IMechE Part H: J. Eng. Med.* 225:831–842, 2011.

e-*Blood*

In vivo imaging of the molecular distribution of the VEGF receptor during angiogenesis in a mouse model of ischemia

Yoh Hamada,[1,2] Kohsuke Gonda,[1] Motohiro Takeda,[1] Akira Sato,[2] Mika Watanabe,[3] Tomoyuki Yambe,[4] Susumu Satomi,[2] and Noriaki Ohuchi[1,5]

[1]Department of Nano-Medical Science, Graduate School of Medicine, Tohoku University, Sendai, Japan; [2]Department of Advanced Surgical Science and Technology, Graduate School of Medicine, Tohoku University, Sendai, Japan; [3]Department of Pathology, Tohoku University Hospital, Sendai, Japan; [4]Department of Medical Engineering and Cardiology, Institute of Development, Aging and Cancer, Tohoku University, Sendai, Japan; and [5]Department of Surgical Oncology, Graduate School of Medicine, Tohoku University, Sendai, Japan

Vascular endothelial growth factor (VEGF) plays a critical role in angiogenesis and has been applied to medical therapy. However, because vascular imaging at the molecular level is impossible, the detailed in vivo dynamics of VEGF and its receptor (VEGFR) remain unknown. In this study, to understand the molecular distribution of VEGF and the VEGFR, we prepared ischemic mice with a new surgical method and induced angiogenesis in the gastrocnemius muscle. Then, we made a VEGF-conjugated fluorescence nanoparticle and performed staining of VEGFR-expressing cells with the fluorescent probe, demonstrating the high affinity of the probe for VEGFR. To observe the physiologic molecular distribution of VEGFR, we performed in vivo single-particle imaging of gastrocnemius in the ischemic leg with the fluorescent probe. The results suggested that only a 3-fold difference of VEGFR distribution is involved in the formation of branched vasculature in angiogenesis, although previous ex vivo data showed a 13-fold difference in its distribution, indicating that a method inducing a several-fold local increase of VEGFR concentration may be effective in generating site-specific angiogenesis in ischemic disease. This new in vivo imaging of ischemic mice could make useful contributions to understanding the mechanisms of angiogenesis and to developing a VEGFR-related drug. (*Blood.* 2011;118(13): e93-e100)

Introduction

Angiogenesis and arteriogenesis play a critical role in neovascularization in adults.[1] Angiogenesis is defined as the sprouting of new capillaries from postcapillary venules,[2] whereas arteriogenesis is defined as the process of artery maturation or the de novo growth of collateral conduits.[3] Our laboratory studies the mechanisms of angiogenesis, and clarification of these mechanisms is crucial for the development of new treatments for arteriosclerotic disorders. Recently, medical applications for recombinant vascular endothelial growth factor (VEGF) proteins or genes have been developed.[4] However, no placebo-controlled trial has yielded overwhelmingly positive results.[1] An understanding of the detailed molecular mechanisms of this angiogenesis factor in vivo is thought to be very important for the effective design of a VEGF-related drug delivery system. However, neither VEGF activity nor VEGFR distribution has been quantitatively analyzed in vivo at a molecular level with respect to therapeutic angiogenesis. In previous animal studies, the efficacy of treatment for atherosclerotic disease was primarily evaluated using angiography, laser Doppler imaging, and the determination of histologic capillary density.[5,6] Angiography can be used to noninvasively visualize vessel size, vessel branching, and the vascular network throughout the body. However, because it is difficult to visualize vascular structures several hundred micrometers beneath the imaging surface, this method is not adequate for the observation of early-stage angiogenesis at a molecular level. Laser Doppler imaging provides a noninvasive measurement of blood flow by determining the Doppler frequency shift of reflected light because of the motion of red blood cells. This technique enables quantitative analysis of improvements in blood flow after injury to the vasculature. However, the Doppler shift measurement is easily influenced by movement artifacts, room temperature, and blood pressure.[7] In addition, it is difficult to analyze microvascular structures using laser Doppler imaging because the resolution of the obtained image is limited by diffusion of the reflected light because of distance between the red blood cells and the detector. Histologic measurements of capillary density can reveal quantitative increases in blood vessel density, and many previous studies have used this metric as a standard evaluation of angiogenesis. However, continuous observation of the same tissue is impossible with this measurement technique as protein structure is influenced by fixation of the tissues. For this reason, histologic techniques are not recommended for physiologic observations of the angiogenesis process. In the aforementioned methods, as resolution is limited to the micrometer level and imaging at the molecular level is currently impossible, the detailed in vivo dynamics of individual VEGF and VEGF receptor (VEGFR) molecules remain unknown. We have developed an in vivo single-particle imaging system using bright and photo-stable fluorescent nanoparticles, or quantum dots (QDs), with a spatial

Submitted December 2, 2010; accepted July 25, 2011. Prepublished online as *Blood* First Edition paper, August 5, 2011; DOI 10.1182/blood-2010-12-322842.

The online version of this article contains a data supplement.

The publication costs of this article were defrayed in part by page charge payment. Therefore, and solely to indicate this fact, this article is hereby marked "advertisement" in accordance with 18 USC section 1734.

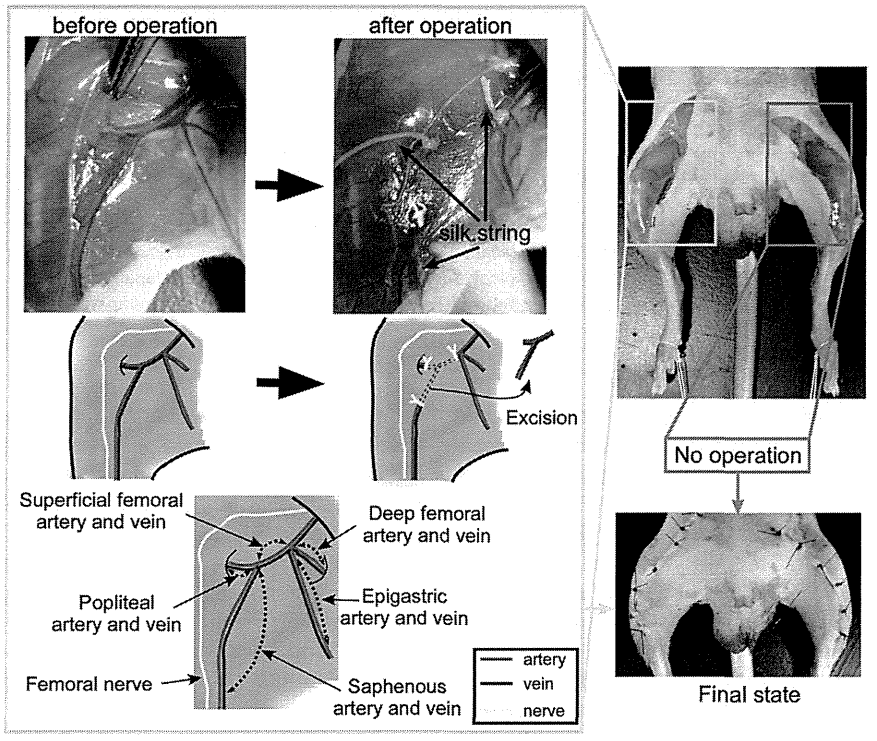

Figure 1. Procedure for preparing the hemi-hind limb ischemic mouse model. On the right leg, we ligated the proximal end of the superficial femoral artery and vein, the origins of the popliteal artery and vein, and the distal portions of the saphenous artery and vein with surgical silk. All vessels surrounding the 3 ligated points were excised. The left leg was not treated, except for an incision in the skin of the thigh.

precision of 7-9 nm. This was performed to clarify the molecular mechanisms of an anti-HER2 antibody-based drug delivery system and of cancer metastasis in tumor-bearing mice.[8,9]

The use of an ischemic mouse model is highly effective for understanding the in vivo molecular dynamics of angiogenic factors and their effects on vascular remodeling. However, 2 surgical concerns impose limitations on previous mouse models.[10] First, angiogenesis and arteriogenesis were not separately evaluated in previous models. As both processes contribute to an increase in the rate of blood flow,[1] it is necessary that the effects of arteriogenesis be eliminated if angiogenesis is to be analyzed. Second, inflammation and edema at the surgical site are known to affect angiogenesis.[11] To overcome these problems, it is critical to establish an improved ischemic mouse model that selectively induces angiogenesis at a specific muscle. Here, we demonstrate the development of an imaging method for determining the molecular distribution of VEGFR labeled with QD-conjugated VEGF. This technique was designed to observe angiogenesis in a novel ischemic mouse model that induces angiogenesis in the gastrocnemius. Our results suggest that only a several-fold difference in VEGFR distribution is required for the promotion of angiogenesis. This novel imaging method may aid in the development of drugs and treatments for atherosclerotic diseases.

Methods

Animals

C57BL/6J male mice (Charles River Laboratories) weighing 20-27 g and 8-9 weeks of age were used for all experiments. All surgical processes were performed under anesthesia with ketamine (100-120 mg/kg) and xylazine (8-10 mg/kg). Anesthesia was maintained for the course of the imaging session. Animals were used in accordance with guidelines approved by the committee on animal experiments of Tohoku University.

Hemi-hind limb ischemic mouse model

The hair of each mouse was removed from the abdomen and both hind limbs with an electric shaver and depilatory cream. The skin from both thighs was then incised to expose the arteries, veins, and nerves. To induce selective ischemia in the gastrocnemius, which is located in the deep layer of the thigh muscles, 3 vessels of the femoral area were ligated in the right hind limb. First, the proximal end of the superficial femoral artery and vein were ligated with surgical silk, size 6-0. Second, the origins of the popliteal artery and vein were ligated. Third, the distal portions of the saphenous artery and vein were ligated to avoid the backflow of blood. Femoral nerves were carefully preserved. Each of the vessels that were surrounded by the 3 ligated points was excised. The left leg was not treated, except for an incision in the skin of the thigh. Finally, the overlying skin was closed (Figure 1).

Histologic capillary density

To confirm that the surgical operation-induced angiogenesis in the gastrocnemius, we performed immunohistologic staining of the muscle with anti-CD31 antibody, a marker for vascular endothelial cells. Mice were killed at predetermined times (7, 14, 21, and 28 days after operation). The gastrocnemius was removed and fixed overnight in 10% formalin in PBS. After fixation, the tissue was embedded in paraffin, and the tissue sections were prepared and mounted on slides. The tissue samples were deparaffinized, and antigen retrieval was performed with proteinase K treatment. After this treatment, the tissue samples were incubated with a rat anti-CD31 monoclonal primary antibody (Angio-Proteomie) at 5 μg/mL for 12 hours at 4°C. After being washed with PBS, the samples were incubated with a biotinylated antirat IgG secondary antibody (Vector Laboratories; 100-fold dilution) for 30 minutes at 25°C. After incubation, the samples were incubated with HRP-conjugated streptavidin (Nidchirei) for 30 minutes at 25°C. Samples were then treated with diaminobenzidine chromogen reagent (Dojindo) and counterstained with hematoxylin. The samples were observed using light microscopy (BX51; Olympus) with an objective lens (×40, 0.75 NA; Olympus) and a camera (DP-25B; Olympus). The images were acquired with image processing software (DP2-BSW Version 1.2).

Laser Doppler perfusion imaging

Blood perfusion of the hind limb was measured using a Laser Doppler Perfusion Imaging system (MoorLDI2-IR; Moor Instruments). This imaging technique provides a noninvasive measurement of blood flow by determining the Doppler frequency shift of light reflected off of moving red blood cells. Mice under the same anesthetic dose described in "Animals" were scanned from the lower abdomen to the end of the toes. After scanning, colored images were obtained with original software (RESEARCH Version 3.09; Moor Instruments). Each pixel in the acquired images reflected an original blood flow value, referred to as a perfusion unit (PU). The mean of the PUs of the lower thighs in a control limb and a treated hind limb was determined. The PUs of ischemic legs were obtained at different time points (before operation, soon after operation, and 7, 14, 21, and 28 days after operation). The relative ratios of the mean PUs between the ischemic and control legs in the same mouse were calculated.

Cell lines

A pancreatic islet endothelial mouse cell line, MS1, was obtained from ATCC. MS1-VEGF cells, which express VEGFR on the cell membrane via the transfection of the VEGF gene, were also acquired from ATCC. These cells were cultured in DMEM (Invitrogen) supplemented with 5% FBS.

Immunostaining of cultured cells with an anti-VEGFR antibody

MS1 and MS1-VEGF cells were cultured on slide glass chambers. After 3 days, the slides were placed in 2.5% formalin in DMEM for 10 minutes. After fixation, the cells were incubated with an anti–mouse VEGFR monoclonal antibody (Pierce Chemical) or a whole mouse IgG (Rockland) primary antibody at 10 μg/mL for 12 hours at 25°C. After the samples were washed with PBS, the cells were incubated with a HRP-conjugated anti–mouse IgG secondary antibody (KPL Europe; 100-fold dilution) for 1 hour at 25°C. After incubation, the samples were treated with diaminobenzidine chromogen reagent and counterstained with hematoxylin. We observed the samples with the same optical system in "Histologic capillary density."

Preparation of angiogenesis factor-conjugated QDs

Mouse VEGF 164 (R&D Systems) and platelet-derived growth factor BB (PDGF; Biovision) were biotinylated using the EZ-Link Micro Sulfo-NHS-LC-Biotinylation Kit (Pierce Chemical). In this reaction, a 1:50 molar ratio of angiogenesis factors and Sulfo-NHS-LC-Biotin was used according to the manufacturer's instructions. The biotinylated VEGF and PDGF were then mixed with avidin-conjugated Qdot705 nanoparticles (QD705; Invitrogen) at a molar ratio of 8:1 or 16:1 and incubated for 1 hour at 25°C. The number of QD705 nanoparticles determined the emission wavelength. QD705-conjugated VEGF and PDGF were termed VEGF-QD and PDGF-QD, respectively.

Single-particle imaging system

The optical system used to observe the fluorescence of the angiogenesis factor-conjugated QDs consisted primarily of an epifluorescent microscope (IX-71; Olympus), a Nipkow disk-type confocal unit (CSU10; Yokogawa), and an EMCCD camera (Ixon DV887; Andor). An objective lens (60×, PlanApo, 1.40 NA; Olympus) was used for imaging. VEGF-QDs were illuminated using a green laser (532 nm; Spectra-Physics). The laser-excited fluorescence of the QDs was filtered with a 695- to 740-nm band-pass filter. Images were obtained at a rate of 5 frames/second. For in vivo imaging, to remove the oscillation because of heartbeats and respiration, a gastrocnemius window was developed and attached to the aforementioned microscopy system.

Single-particle imaging of VEGF-QDs in cultured cells

To investigate the affinity of VEGF-QDs for VEGFR, MS1, and MS1-VEGF, cells were incubated with 1, 10, or 50nM VEGF-QDs for 1 hour at 25°C. After 3 washes with DMEM, these cells were observed in a glass-bottom dish using the single-particle imaging system. The fluorescence intensities of QD signals from the cells were analyzed as gray values using ImageJ 1.38 software (www.rsb.info.nih.gov/ij). The gray values of 100 frames (200 milliseconds/frame) from a single cell were averaged, and the gray value of the background was subtracted from that of the cell. The mean gray value per pixel in the background-subtracted image of the cell was multiplied by the total number of pixels making up the image of the cell. The total fluorescence intensity of the QDs per cell was thus determined. In the 10nM VEGF-QD treatment, QD fluorescence signals were clearly observed on MS1-VEGF cells. In contrast, when MS1-VEGF cells were incubated with 1nM VEGF-QDs, the QD fluorescence signals were low. When the cells were treated with 50nM VEGF-QDs, QD signals were exceedingly high or even saturated (data not shown). In MS1 cells incubated with various concentrations of VEGF-QDs, the VEGF-QD fluorescence signals were very low. These results indicate that VEGF-QDs specifically recognize VEGFR and that the 10nM concentration was appropriate for imaging the binding of VEGF-QDs to VEGFR. Moreover, to provide stronger evidence of the affinity of VEGF-QDs for VEGFR, MS1, and MS1-VEGF, cells were incubated with 10nM unconjugated QDs, PDGF-QDs, or VEGF-QDs for 1 hour at 25°C, and the resulting fluorescence intensities were examined.

In vivo fluorescence imaging with the IVIS Spectrum system

To confirm that VEGF-QDs accumulated in the ischemic leg, we performed in vivo fluorescence imaging using the IVIS Spectrum imaging system (Caliper Life Sciences) at 4, 9, and 14 days after preparation of ischemic model mice. Unconjugated QDs or VEGF-QDs were injected intracardially into the mice. The final concentration of the QD probes in the blood was 10nM, as determined by the single-particle imaging data from cultured cells. The detection sensitivity of the fluorescent signal using the IVIS Spectrum is poorer than the single-particle imaging system but allows for noninvasive visualization of the whole body of the mouse. Therefore, fluorescence images were taken 10 minutes after injection of fluorescent probes, before the fluorescence signals decreased, because of their washing out with the blood. Fluorescence intensities of the QDs were analyzed using accessory software (Living Image Version 4.0; Caliper Life Sciences). For data analyses, the relative ratio of fluorescence between the ischemic and control leg of the same mouse was calculated.

Single-particle imaging of VEGF-QDs in the gastrocnemius of ischemic model mice

To examine the distribution of VEGF-QDs in the gastrocnemius of the ischemic leg, we performed in vivo single-particle imaging of the vasculature 4, 9, and 14 days after operation. The skin of the ischemic leg was opened to expose the thigh muscles. The skin of the hind limbs was then fixed to a plastic plate using suture thread and Superglue. Use of Superglue made both connections of the skin to the plate more stable without damaging the vasculature, eliminating the background oscillations from the heartbeat and respiration during observation. To expose the gastrocnemius, the skin and hemimembranous muscle, which is located on the superficial layer of the gastrocnemius, were then removed. The mouse, which was mounted as described on the plastic plate, was then fixed to a hand-made aluminum stage designed to stabilize the plate with screws. Unconjugated QDs or VEGF-QDs were injected intracardially into the mice. The sensitivity of the single-particle imaging system to the fluorescence signal is extremely high; and immediately after injection, a part of probes are free in the blood and have not bound to VEGFR. This initially prevents observation of the interaction between the VEGF-QDs and VEGFR on the vascular wall. Therefore, in vivo single-particle imaging of the fluorescent probes was carried out 1 hour after injection. By this time, the concentration of the free probe in the blood was decreased. To quantitatively measure the affinity of the VEGF-QDs for the vasculature, an analysis was performed as follows. A total of 100 frames, each 512 pixels square and representing an exposure of 200 milliseconds, were overlaid using image processing software (G-count 1.01; G-angstrom). A portion of the overlaid (192 pixels square) image was examined to determine the number of QD particles in proper-sized vasculature. For each image analyzed, the fluorescence intensity (as gray values) of QD signals from the tissues was determined using ImageJ software. The mean gray value, derived from the tissues'

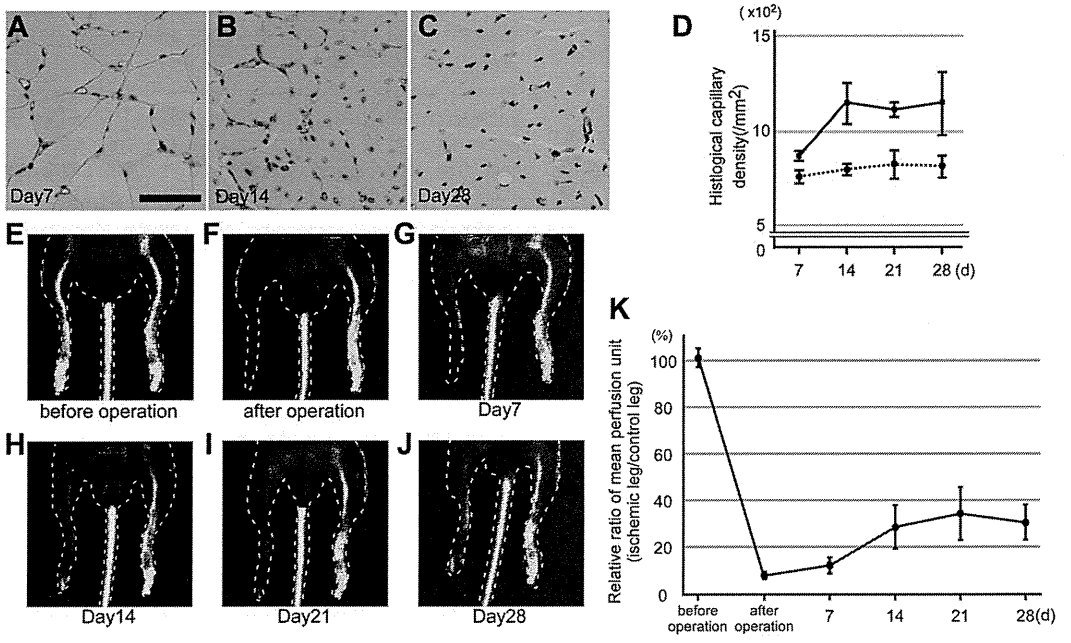

Figure 2. Evaluation of angiogenesis of the ischemic model mice. (A-C) Typical images of the gastrocnemius immunostained with an anti-CD31 antibody. The muscles from ischemic legs were isolated at 7, 14, and 28 days after the induction of ischemia and immunostained. Brown circles and dots represent $CD31^+$ capillaries. Scale bar represents 50 μm. (D) Measurement of $CD31^+$ capillary density. In the gastrocnemius of the ischemic or control leg, capillaries stained with the anti-CD31 antibody were counted. Solid and dotted lines represent the sample derived from ischemic and control legs, respectively. n = 4. Error bars represent SEM. (E-J) Changes in blood perfusion were assessed using laser Doppler perfusion imaging in ischemic legs of model mice. (E-F) Images before and soon after operation. After operation, the perfusion signal in the ischemic leg is significantly decreased. (G-J) Images from 7, 14, 21, and 28 days after operation. Blood perfusion in an ischemic leg gradually increases. (K) Change in perfusion units as determined by this imaging technique. Relative ratios of mean perfusion units between ischemic and control legs in the same mouse are shown (ischemic leg value/control leg value). n = 6. Error bars represent SEM.

autofluorescence per pixel, was subtracted from the fluorescence value of the vascular wall area. The resulting gray value was then multiplied by the total number of pixels of the vascular wall. This value reflected the total fluorescence intensity of all QDs bound to the vascular wall (total QD value).

To precisely determine the number of QD particles on the vascular wall, it was necessary to define the fluorescence intensity of a single QD. Because QDs that fluoresce at the same wavelength are uniform in size, QD705 fluorescence intensity is proportional to the particle number. Moreover, the QD fluorescence is composed of fluorescent and nonfluorescent states referred to as on- and off-states. This property results in blinking of a QD. When the fluorescence and other properties of QD particles were analyzed immediately after their purchase, we determined that the mean duration of the off-state over 20 seconds was approximately 4 seconds and that the calculated SEM was very low.[12] In cases where QDs aggregate, the mean duration of the off-state per unit time is shortened because the on- and off-states of each particle in the aggregate occur randomly. Therefore, based on an off-state duration of 4 seconds, we selected a single particle QD from each image and measured the fluorescence intensity of the single QD particle (single QD value) in the same manner as the total QD value. The total QD value was divided by a single QD value, and the number of QD particles per 10 μm of vascular wall was calculated.

Statistical analysis

Data are mean ± SEM. An F test was performed and equal variance was defined as P values ≥ .05. Comparisons between groups were performed using the parametric Student t test (≥ .05 at F test) or Welch t test ($P < .05$ at F test). $P < .05$ was considered significant for both t tests.

Results

Induction of angiogenesis in ischemic model mice

To induce angiogenesis at a selected site and to eliminate the effects of inflammation and edema,[11] we targeted the gastrocnemius. This muscle is primarily supplied by the popliteal and saphenous arteries, and no remarkable collateral arteries exist near the muscle. We therefore ligated the popliteal and saphenous arteries to induce angiogenesis in the gastrocnemius (Figure 1). Other muscles in the thigh are primarily supplied by the deep femoral artery, which was maintained as a collateral artery after the surgery. Therefore, we think that our surgery is appropriate for analyses of angiogenesis mechanisms. The gastrocnemius is located deep among the thigh muscles, and the skin and semimembranosus muscle located on the upper layer of the gastrocnemius were removed just before in vivo imaging. Therefore, we avoided the effects of inflammation and edema-induced factors on normal angiogenesis. To determine whether the number of capillaries in the gastrocnemius of ischemic legs increased, we histologically determined the capillary densities over time (Figure 2A-C). Capillary densities in the control legs did not significantly change during observation (Figure 2D). In contrast, the capillary densities in ischemic legs increased gradually over 14 days, peaked at day 14, and were steady between day 14 and day 28. This finding demonstrates that angiogenesis was induced in the ischemic leg (Figure 2D). To investigate improvement of blood flow in the model mice using another method, we evaluated the change in blood flow using laser Doppler perfusion imaging (Figure 2E-J). The relative ratio of the mean PU between ischemic and control legs in the same mouse (ischemic leg value/control leg value) decreased to ~ 8% soon after operation (Figure 2E-F,K). This ratio then increased to ~ 34% 21 days after the surgery (Figure 2I,K). Both observations indicate that angiogenesis was effectively induced in the gastrocnemius between 7 days and 14 days after the procedure. The slight difference in the rate of increase of perfusion between the 2 imaging methods may be because the laser Doppler perfusion imaging analyzed the thigh as a whole, and arteriogenesis induced by inflammation and

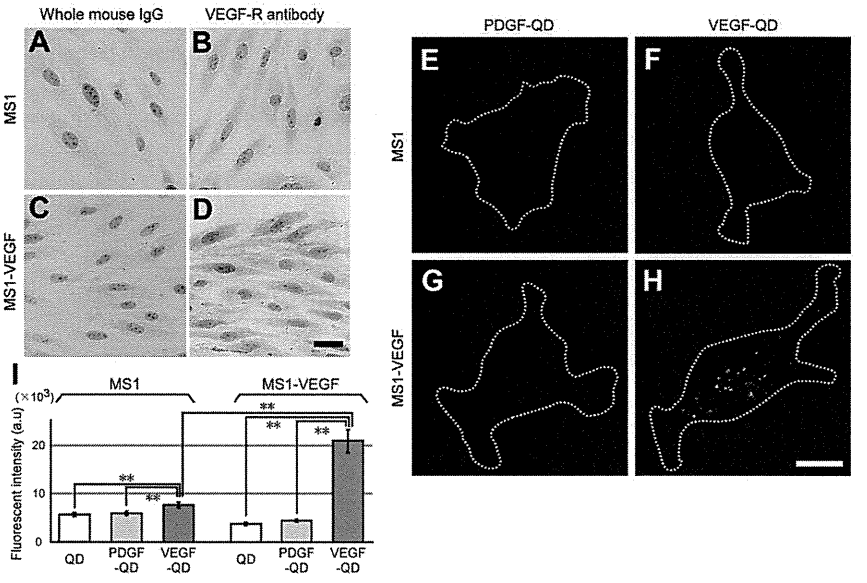

Figure 3. VEGFR distribution in MS1 and MS1-VEGF cells and the affinity of angiogenesis factor-conjugated QDs to these cell lines. (A-D) Immunostaining of MS1 and MS1-VEGF cells with an anti-VEGFR antibody. Scale bar represents 50 μm. (E-H) Typical images of cells treated with fluorescent particles. MS1 and MS1-VEGF cells were treated with unconjugated QDs, PDGF-QDs, or VEGF-QDs. Representative images are shown of cells treated with PDGF-QDs and VEGF-QDs. Data from cells treated with unconjugated QDs are not shown. White dots represent fluorescent QDs; and white dotted lines, the outline of the cell. Scale bar represents 10 μm. (I) QD fluorescence intensity per cell. The fluorescence intensity of QD signals from the cells was analyzed as gray values. In each condition, n = 30. $^{**}P < .01$. Error bars represent SEM.

edema of the semimembranous muscle may have occurred in this larger volume.

Preparation and characterization of VEGF-QDs

To visualize the molecular distribution of VEGF using single-particle imaging, VEGF was conjugated with QDs (VEGF-QD). PDGF-conjugated QDs (PDGF-QD) were also prepared as control probes (supplemental Figure 1, available on the *Blood* Web site; see the Supplemental Materials link at the top of the online article). To examine the binding of VEGF-QD and VEGFR, staining was performed on MS1 and MS1-VEGF cells treated with unconjugated QDs, PDGF-QDs, and VEGF-QDs. High levels of VEGFR expression in MS1-VEGF cells were confirmed by immunostaining with an anti-VEGFR antibody (Figure 3C-D), whereas low-level expression was observed in MS1 cells (Figure 3A-B). The analyses of QD-probe fluorescence indicated that the total fluorescence intensity of VEGF-QDs in MS1-VEGF cells was 21.0 ± 2.4 × 10^4 (Figure 3H-I). This value was remarkably higher than the observed fluorescence values of stained MS1-VEGF cells treated with unconjugated QDs or PDGF-QDs (unconjugated QDs, 3.8 ± 0.3 × 10^4; PDGF-QDs, 4.4 ± 0.3 × 10^4; Figure 3G,I) and those of MS1 cells treated with unconjugated QDs, PDGF-QDs, or VEGF-QDs (unconjugated QDs, 5.7 ± 0.4 × 10^4; PDGF-QDs, 6.0 ± 0.4 × 10^4; VEGF-QDs, 7.7 ± 0.6 × 10^4; Figure 3E-F,I). These results demonstrate that VEGF-QDs bind specifically to VEGFR.

In vivo distribution of VEGFR labeled with VEGF-QDs

To determine the distribution of VEGFR labeled with VEGF-QDs during angiogenesis, we performed 2 in vivo fluorescence imaging techniques. In these imaging protocols, we examined ischemic model mice at 4, 9, and 14 days after operation to analyze in detail the changes in VEGFR distribution over time. Imaging performed with the IVIS Spectrum system has the advantage of imaging the fluorescence of the entire body of the mouse, although the spatial precision of this technique is low. To simultaneously observe the fluorescence of both ischemic and control legs after injection of unconjugated QDs or VEGF-QDs into the model mice, the IVIS Spectrum system was used (Figure 4A-D). Individual mice exhibit different degrees of autofluorescence. The relative ratio of fluorescence between the ischemic and control leg in each mouse was therefore calculated (ischemic leg fluorescence/control leg fluorescence). In model mice at 4 days after operation, the relative fluorescence ratio resulting from injection of unconjugated QDs was 0.71 ± 0.01, and the ratio after injection of VEGF-QDs was 0.72 ± 0.03 (Figure 4E). These results indicate that VEGF-QDs did not selectively accumulate in the ischemic legs at the time of

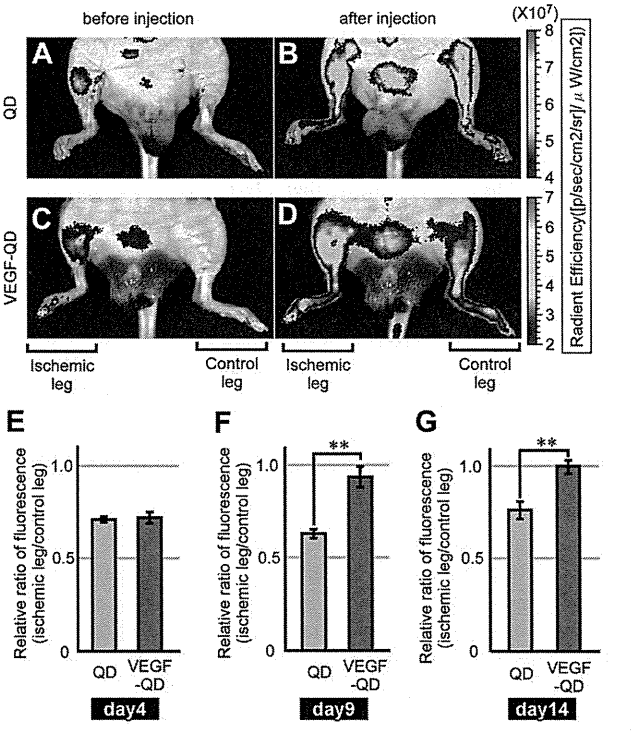

Figure 4. In vivo fluorescence imaging of the ischemic model mice using the IVIS Spectrum system. (A-D) Images using IVIS Spectrum. Unconjugated QDs and VEGF-QDs were injected intracardially into the model mice. Mice were illuminated with light with a wavelength of 625-655 nm. Excited fluorescence was filtered with a 690- to 710-nm wavelength band-pass filter. (E-G) The relative ratios of fluorescence between ischemic and control legs in mice at 4 days (E), 9 days (F), and 14 days (G) after operation. The fluorescence intensity of the ischemic leg divided by that of the control leg was calculated (ischemic leg fluorescence/control leg fluorescence). n = 5. Error bars represent SEM. $^{**}P < .05$.

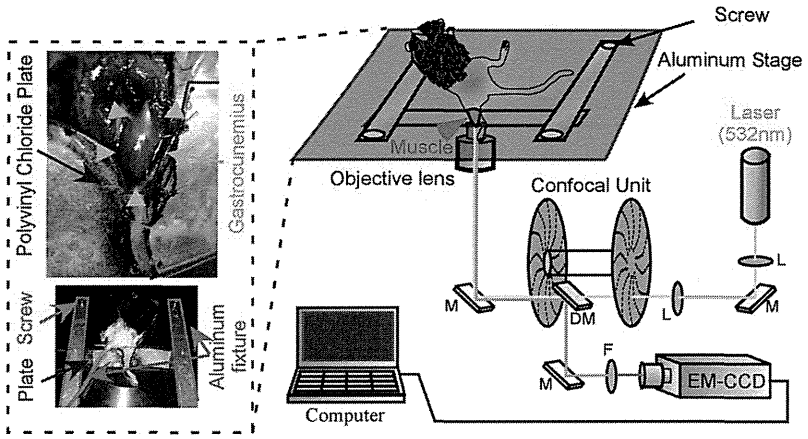

Figure 5. Schematic of the in vivo single-particle imaging system. An ischemic leg of a model mouse was stabilized on a polyvinyl plate using suture thread and instant Superglue. The skin and hemimembranous muscle were then removed. The gastrocnemius was selectively imaged using a single-particle imaging system.

measurement. In contrast, at 9 and 14 days after operation, the relative ratios resulting from injection of unconjugated QDs were 0.65 ± 0.02 and 0.76 ± 0.05, respectively, whereas the observed ratios after injection of VEGF-QDs were 0.94 ± 0.06 and 1.00 ± 0.04, respectively (Figure 4F-G), suggesting that VEGF-QDs accumulated in the ischemic leg to a greater degree than in the control leg at the time of measurement.

In addition to using the IVIS system, we also conducted in vivo single-particle imaging. For this protocol, we developed surgical fixation methods of mice beyond that in our previous imaging method. In particular, we designed a polyvinyl chloride plate with a window fit to the shape of the gastrocnemius. The skin around the gastrocnemius was bound to the plate with suture thread and Superglue (Figure 5). These improvements eliminated background oscillations because of the heartbeat and respiration, enabling us to observe the physiologic angiogenesis that sustains blood flow after ischemia (supplemental Movies 1, 2). We observed the distribution of unconjugated QDs or VEGF-QDs after injection of the respective probe. The results indicate that a large number of VEGF-QDs were specifically localized on the vessel walls in ischemic legs (Figure 6A-H), whereas fluorescence after injection of unconjugated QDs was very weak (supplemental Figure 2A-D). We measured the total fluorescence intensity resulting from all QDs on the vascular wall (total QD value) and the fluorescence intensity of single QD (single QD value) as gray values. The total QD value was then divided by the single QD value, and the number of QD particles per 10 μm of the vascular wall was calculated (Figure 6I; supplemental Figure 2E). These analyses revealed that QD fluorescence on the vascular wall was weak in both ischemic and control legs in mice injected with unconjugated QDs (supplemental Figure 2E). When VEGF-QDs probe were injected at 4 days after operation, the number of VEGF-QDs on the vascular walls of ischemic legs was similar to the number observed in control legs. Moreover, there was no difference in number of particles on the walls of branched or linear vasculature in ischemic legs (Figure 6C-D,I). In contrast, the number of VEGF-QDs in the branched vasculature in ischemic legs was 3.4-fold greater than the number of VEGF-QDs in the linear vasculature 9 days after operation (Figure 6E-F,I) and 4.5-fold greater than the number of VEGF-QDs in the branched vasculature in control legs (Figure 6B,F,I). Fourteen days after operation, the number of VEGF-QDs on the walls of the branched vasculature in ischemic legs was 3.3-fold greater than the number of particles on the walls of the linear vasculature (Figure 6G-I) and 4.3-fold greater than the number of VEGF-QDs in the branched vasculature in control legs (Figure 6I). These results demonstrate that our single-particle imaging method is able to quantitatively describe the in vivo distribution of VEGFR labeled with VEGF-QDs during angiogenesis in ischemic legs.

Discussion

In vivo molecular imaging using high spatial precision in ischemic model mice is highly effective for the quantitative description of the molecular dynamics of VEGF and VEGFR during angiogenesis. This information can be applied to the development of treatments for ischemic disease. Previously described mouse models suffered from surgical limitations. These difficulties involved: (1) the induction of angiogenesis without arteriogenesis, an effect of arteries that remains after surgery; and (2) the induction of inflammation and edema during surgery.[10] We focused on the gastrocnemius, which is located deep in the thigh, and developed a new ischemic mouse model consisting of the ligation of 3 pairs of vessels: the superficial femoral, popliteal, and saphenous arteries and veins (Figure 1). We confirmed that angiogenesis was effectively induced in the model mice using conventional evaluation methods, histological capillary density measurements, and laser Doppler imaging (Figure 2D,K).

We have previously described the development of in vivo single-particle imaging using QDs with a spatial precision of 7-9 nm to clarify the molecular mechanisms of a anti-HER2 antibody-based drug delivery system and cancer metastasis in tumor-bearing mice.[8,9] In previous studies, in vivo imaging with high spatial precision was not applied to the visualization of angiogenesis. For this application in the current studies, we further modified our surgical fixation method (Figure 5). For the imaging technique used here, we designed a polyvinyl chloride plate with a window fit to the shape for the gastrocnemius. This window enabled us to observe the physiologic angiogenesis during active blood flow. We observed the in vivo molecular distribution of VEGF-QDs using this improved imaging in ischemic mice at 4, 9, and 14 days after a surgery in which angiogenesis in the gastrocnemius was effectively induced. The results demonstrate that a large number of VEGF-QDs specifically localized to the vessel wall in ischemic legs (Figure 6A-H), whereas fluorescence resulting from unconjugated QDs at the wall was very weak (supplemental Figure 2A-D). To quantitatively analyze the molecular distribution of VEGF-QD-labeled VEGFRs, we measured the total number of QDs

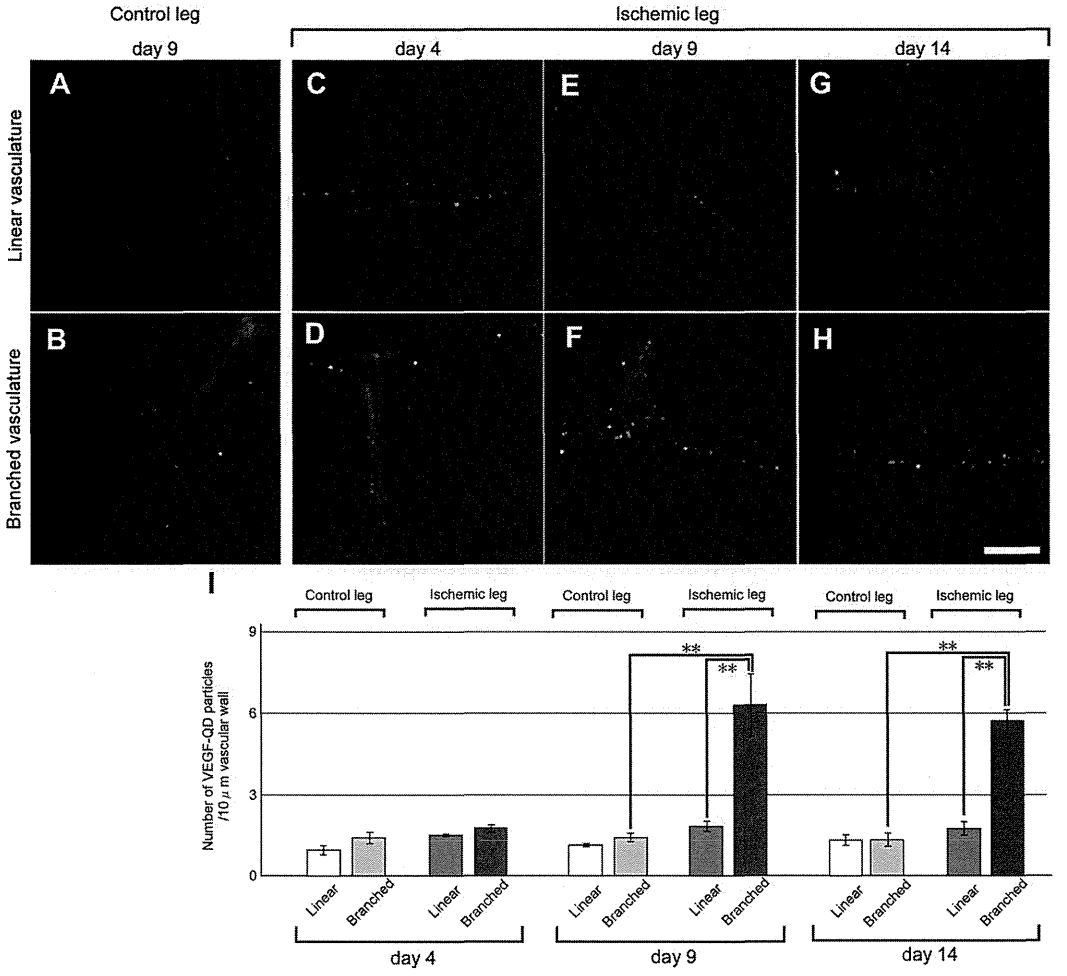

Figure 6. In vivo imaging of unconjugated and VEGF-QDs during angiogenesis in ischemic legs. (A-H) Typical images of vasculature in control and ischemic legs. These images were generated by overlaying 100 frames (200 ms/frame), each consisting of a 192-pixel square image, using Adobe after effect CS4 9.0.3 software. In model mice injected with VEGF-QDs, we observed "linear vasculature" (A,C,E,G) and "branched vasculature" (B,D,F,H) in control and ischemic mouse legs at 4, 9, and 14 days after operation. The data from unconjugated QDs are not shown (supplemental Figure 2). White dots represent QD fluorescence. Scale bar represents 10 μm. (I) The number of VEGF-QDs in different types of vasculature. The number of fluorescent particles per 10 μm of the vascular wall is quantified. n = 4. $^{**}P < .05$. Error bars represent SEM.

(Figure 6I; supplemental Figure 2E). Because QDs with the same fluorescence wavelength are uniform in size, the fluorescence intensity of the QDs is proportional to the number of particles.[12] This property enabled us to determine relative VEGFR expression levels with a very high degree of accuracy. In mice 4 days after operation, there were no significant differences between the branched vasculature and the linear vasculature (Figure 6C-D,I). Furthermore, the IVIS Spectrum data from this time point did not show a significant difference in the accumulation of unconjugated QDs or VEGF-QDs in ischemic legs (Figure 4E). These data indicate that any VEGFR redistribution induced by hypoxic stimulation in ischemic legs occurs only at low levels at this time point. In mice at 9 days after operation, the data demonstrate a 3.4-fold greater number of VEGF-QDs on the walls of branched vasculature in ischemic legs than on the walls of linear vasculature in these legs and a 4.5-fold greater number than on the branched vasculature of control legs in model mice (Figure 6I). In mice at 14 days after operation, the data revealed that the number of VEGF-QDs on the walls of branched vasculature in ischemic legs was 3.3-fold greater than that on the linear vasculature in ischemic legs and 4.3-fold greater number than the number of VEGF-QDs on the branched vasculature in control legs in model mice (Figure 6I). These results demonstrate that the data acquired from mice at 9 and 14 days after operation using the single-particle imaging technique were similar to data acquired using the IVIS Spectrum system (Figure 4F-G). From the data, it appears that the VEGFR protein expression on the branched vasculature in ischemic legs increases gradually between day 4 and day 9 via hypoxic stimulation, peaks at approximately day 9, and remains steady from day 9 to day 14. Histologic capillary density data reveal that capillary densities in ischemic legs increase gradually over 14 days (Figure 2D). It is very interesting, therefore, that the peak of VEGFR expression occurred ~ 9 days after the procedure. Furthermore, these data suggest that only a several-fold increase in the expression level of VEGFR on endothelial cells is critical for angiogenesis in ischemic tissues.

During angiogenesis, tip cells, stalk cells, and phalanx cells control vessel sprouting. Tip cells are located at the forefront of the sprouting vessel, stalk cells are located behind the tip cell at the branch, and phalanx cells are found in the unbranched endothelial layer.[13] Previous ex vivo studies reported that VEGFR expression in the tip cell is high to sense the VEGF concentration gradient in the extravascular area. In stalk cells, which control elongation of a new branch, VEGFR levels are lower than in the tip cells.[14] In phalanx cells, which normalize the endothelial cell layer, VEGFR levels are lower than in the stalk cells.[13] However, these are

qualitative data, and a quantitative analysis of the VEGFR distribution required to regulate the behavior of these cells has not been carried out in vivo. In addition, previous ex vivo data revealed that the amount of VEGFR protein involved in angiogenesis in ischemic tissue is 13-fold greater than in normal tissues.[15] In this report, however, because the total amount of VEGFR in both the vessel wall and the extravascular area was measured, the detailed quantitative distribution of VEGFR was not known. Our results suggest that only an approximately 3-fold difference in VEGFR distribution on the vascular wall is involved in the formation of branched vasculature from linear vasculature during angiogenesis (Figure 6I). The increase in VEGFR levels we observe after ischemia may quantitatively reveal a gradient of VEGFR expression levels between the stalk cells and pharynx cells.

Our results indicate that VEGFR distribution in in vivo ischemic tissues increased gradually over a specific period and remained steady at an approximately 3-fold increase. To increase the number of sprouting vessels for the operation of ischemic hypoxia, the steady several-fold increase of VEGFR expression levels at the ischemic site may be effective for controlled angiogenesis. Previously, treatment against ischemic hypoxia using VEGF gene therapy induced only a slight increase in VEGF blood concentrations.[16] In addition, overexpression of VEGF produces abnormal vessels in tumor angiogenesis.[17] These results suggest that in the context of ischemia, it is difficult to site-specifically modulate the concentration of a VEGF-related therapeutic to an appropriate value. Therefore, next-generation therapies targeting VEGFR, in addition to VEGF, may effectively induce site-specific angiogenesis for the treatment of ischemic disease. The novel in vivo imaging technique described here for the analysis of ischemic model mice may increase the understanding of the mechanisms of angiogenesis and aid in the development of VEGFR-related therapies.

Acknowledgments

The authors thank Yohei Hamanaka, Takayuki Nakagawa, Masaaki Kawai, and Makoto Hikage for helpful discussion and Yayoi Takahashi and Yasuko Furukawa for technical assistance.

This work was supported by the Japan MEXT (Grants-in-Aid for Scientific Research in Priority Areas; N.O. and K.G.), a Grant-in-Aid for a Research Project, Promotion of Advanced Medical Technology (H18-Nano-001) from the Ministry of Health, Labor and Welfare of Japan (N.O.), and Research for Promoting Technological Seeds of JST (K.G.). This work was also supported by the Biomedical Research Core of Tohoku University Graduate School of Medicine, Tohoku University Global COE Program "Global Nano-Biomedical Engineering Education and Research Network Center," Core Research for Evolutional Science and Technology of JST, and Konica Minolta Medical & Graphic Inc.

Authorship

Contribution: Y.H. and K.G. designed and performed the research, analyzed the data, and wrote the manuscript; M.T., A.S., and N.O. performed research and analyzed data; M.W. and S.S. performed research; and T.Y. provided the equipment for laser Doppler perfusion imaging and performed research.

Conflict-of-interest disclosure: K.G. and M.T. have received a research grant from Konica Minolta Medical & Graphic Inc. N.O. has received research grants from Takeda Pharmaceutical Company Limited and Konica Minolta Medical & Graphic Inc. The remaining authors declare no competing financial interests.

Correspondence: Kohsuke Gonda, Department of Nano-Medical Science, Graduate School of Medicine, Tohoku University, Seiryo-machi, Aoba-ku, Sendai 980-8575, Japan; e-mail: gonda@med.tohoku.ac.jp.

References

1. Simons M. Angiogenesis: where do we stand now? *Circulation.* 2005;111(12):1556-1566.
2. Carmeliet P. Angiogenesis in life, disease and medicine. *Nature.* 2005;438(7070):932-936.
3. Helisch A, Schaper W. Arteriogenesis: the development and growth of collateral arteries. *Microcirculation.* 2003;10(1):83-97.
4. Simons M, Ware JA. Therapeutic angiogenesis in cardiovascular disease. *Nat Rev Drug Discov.* 2003;2(11):863-871.
5. Gowdak LHW, Poliakova L, Wang XT, et al. Adenovirus-mediated VEGF(121) gene transfer stimulates angiogenesis in normoperfused skeletal muscle and preserves tissue perfusion after induction of ischemia. *Circulation.* 2000;102(5):565-571.
6. Lu YX, Shansky J, Del Tatto M, Ferland P, Wang XY, Vandenburgh H. Recombinant vascular endothelial growth factor secreted from tissue-engineered bioartificial muscles promotes localized angiogenesis. *Circulation.* 2001;104(5):594-599.
7. Sakr Y. Techniques to assess tissue oxygenation in the clinical setting. *Transfus Apher Sci.* 2010;43(1):79-94.
8. Gonda K, Watanabe TM, Ohuchi N, Higuchi H. In vivo nano-imaging of membrane dynamics in metastatic tumor cells using quantum dots. *J Biol Chem.* 2010;285(4):2750-2757.
9. Tada H, Higuchi H, Wanatabe TM, Ohuchi N. In vivo real-time tracking of single quantum dots conjugated with monoclonal anti-HER2 antibody in tumors of mice. *Cancer Res.* 2007;67(3):1138-1144.
10. Couffinhal T, Silver M, Zheng LP, Kearney M, Witzenbichler B, Isner JM. Mouse model of angiogenesis. *Am J Pathol.* 1998;152(6):1667-1679.
11. Limbourg A, Korff T, Napp LC, Schaper W, Drexler H, Limbourg FP. Evaluation of postnatal arteriogenesis and angiogenesis in a mouse model of hind-limb ischemia. *Nat Protoc.* 2009;4(12):1737-1748.
12. Hikage M, Gonda K, Takeda M, et al. Nano-imaging of the lymph network structure with quantum dots. *Nanotechnology.* 2010;21:18.
13. Carmeliet P, De Smet F, Loges S, Mazzone M. Branching morphogenesis and antiangiogenesis candidates: tip cells lead the way. *Nat Rev Clin Oncol.* 2009;6(6):315-326.
14. Gerhardt H, Golding M, Fruttiger M, et al. VEGF guides angiogenic sprouting utilizing endothelial tip cell filopodia. *J Cell Biol.* 2003;161(6):1163-1177.
15. Lu EX, Wagner WR, Schellenberger U, et al. Targeted in vivo labeling of receptors for vascular endothelial growth factor: approach to identification of ischemic tissue. *Circulation.* 2003;108(1):97-103.
16. Tongers J, Roncalli JG, Losordo DW. Therapeutic angiogenesis for critical limb ischemia: microvascular therapies coming of age. *Circulation.* 2008;118(1):9-16.
17. Jain RK. Normalization of tumor vasculature: an emerging concept in antiangiogenic therapy. *Science.* 2005;307(5706):58-62.

Ultrasound Obstet Gynecol 2013; 42: 112–114
Published online in Wiley Online Library (wileyonlinelibrary.com). DOI: 10.1002/uog.12466

First successful case of non-invasive *in-utero* treatment of twin reversed arterial perfusion sequence by high-intensity focused ultrasound

T. OKAI*, K. ICHIZUKA*, J. HASEGAWA*, R. MATSUOKA*, M. NAKAMURA*, K. SHIMODAIRA*, A. SEKIZAWA*, M. KUSHIMA† and S. UMEMURA‡

**Department of Obstetrics and Gynecology, School of Medicine, Showa University, Tokyo, Japan; †Department of Pathology, School of Medicine, Showa University, Tokyo, Japan; ‡Graduate School of Biomedical Engineering, Tohoku University, Sendai, Japan*

KEYWORDS: fetal therapy; HIFU; TRAP sequence

ABSTRACT

High-intensity focused ultrasound (HIFU) has excellent potential as a non-invasive therapeutic tool in various fields of medicine. We present a case of twin reversed arterial perfusion sequence, in which non-invasive blood flow occlusion in the acardiac fetus was successfully achieved by means of HIFU exposure from outside the maternal abdomen. HIFU was applied to blood vessels of the acardiac fetus at the point at which the umbilical cord entered the body in a series of four procedures at 3-day intervals starting at 13 weeks' gestation, and in a final procedure with higher power at 17 weeks. The HIFU intensity was set at approximately 2300 W/cm^2 for the initial series of procedures and at 4600 W/cm^2 for the final procedure, with exposure periods of 10 s. As color Doppler examination revealed absence of blood flow to the acardiac fetus after the second round of HIFU exposure, we concluded that complete occlusion of target vessels had been achieved. Delivery was by Cesarean section at 37 weeks' gestation. A male neonate (the pump fetus) was born weighing 1903 g with Apgar scores of 8 and 9 at 1 and 5 min, respectively. At the time of writing, the baby was healthy and growing normally, with the exception of congenital pseudarthrosis. Copyright © 2013 ISUOG. Published by John Wiley & Sons Ltd.

CASE REPORT

A 32-year-old woman, gravida 1 para 0, who was pregnant with twins, was referred to our hospital because of the absence of a heart beat in one fetus. Based on the ultrasonographic findings, we diagnosed twin reversed arterial perfusion (TRAP) sequence. Following ethics committee approval and counseling of the patient, which included a thorough explanation of the procedure as well as the possible adverse effects on the mother and pump fetus and the results of our previous case[1], we conducted high-intensity focused ultrasound (HIFU) treatment (Figure 1). The aim of HIFU was to non-invasively occlude blood flow in the acardiac fetus with the aim of diminishing the cardiac burden in the normal 'pump' fetus.

The HIFU transducer used in this case was a prototype developed by us with a resonant frequency of 1.71 MHz, a spherical radius of curvature of 60 mm, and a focal length of 60 mm. The exposure method and conditions were derived from the findings of our previous animal experiments[2,3] and the first clinical case[1]. The blood vessel of the acardiac fetus at the point at which the umbilical cord entered the body was targeted for HIFU exposure through the maternal abdomen.

HIFU irradiation was conducted at 13 + 5 weeks' gestation. The HIFU intensity at the focused area (3.6 mm^2) was set at approximately 2300 W/cm^2 with exposure times of 10 s repeated several times. Following this first round of irradiation, blood flow in the aorta of the acardiac fetus became very weak. However, the following day blood flow had recovered to its preoperative state (Figure 2a). The patient did not suffer any adverse events from the procedure, and she opted for a series of repeat procedures. We conducted three more courses of HIFU exposure in a similar manner at 3-day intervals. However, the results were similar to that of the first procedure. At 17 + 5 weeks' gestation, we decided to increase the emission power of the HIFU and performed the procedure at a higher power of 4600 W/cm^2. This resulted in cessation of blood flow in the acardiac fetus and its umbilicus the following day, indicating complete occlusion (Figure 2b).

Correspondence to: Dr K. Ichizuka, Showa University, School of Medicine, Department of Obstetrics and Gynecology, 142–8666 Hatanodai, Shinagawa-ku, Tokyo, Japan (e-mail: k.ichizuka@me.com)

Accepted: 14 March 2013

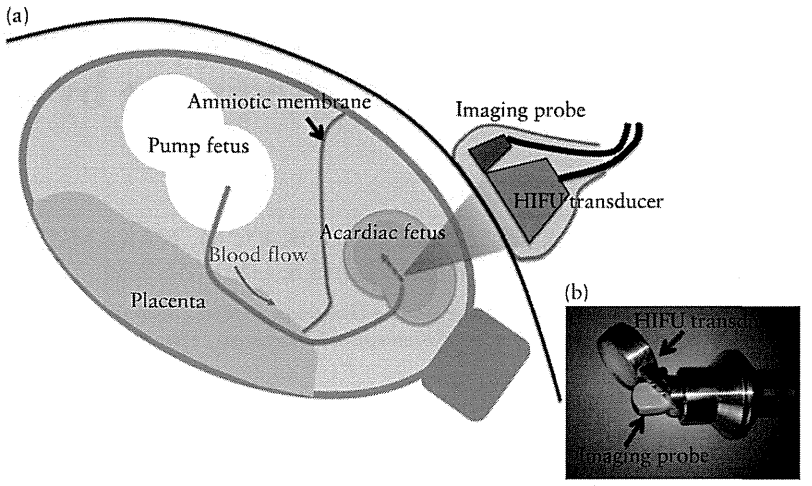

Figure 1 (a) Schematic diagram showing application of high-intensity focused ultrasound (HIFU) in a case of twin reversed arterial perfusion sequence and (b) photograph of HIFU transducer and imaging probe, which were applied after placing in a plastic bag filled with degassed water.

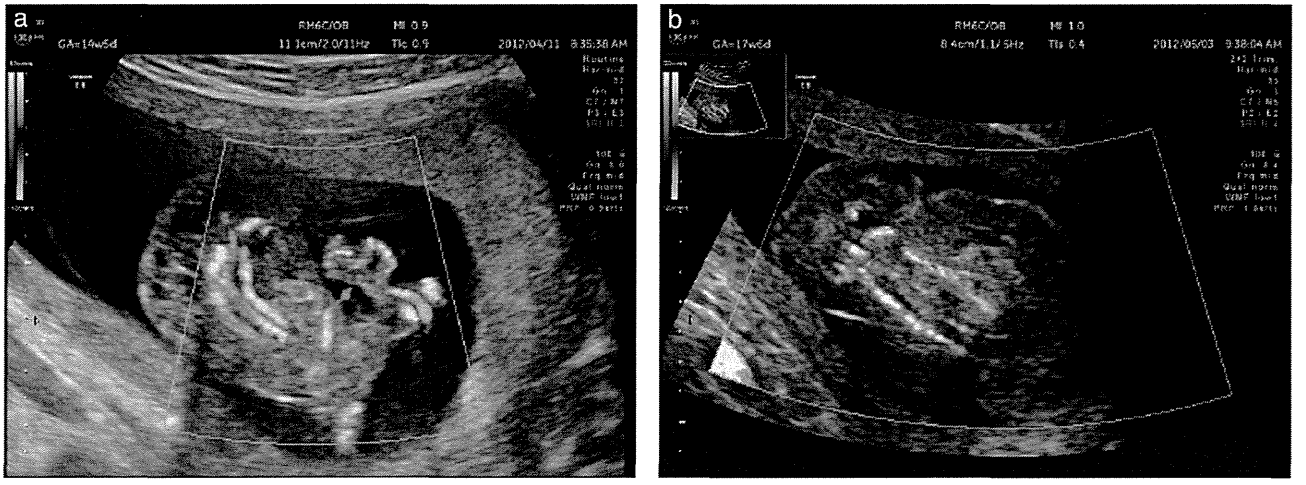

Figure 2 Color Doppler ultrasound images of acardiac fetus at 14 + 5 weeks' gestation, after initial series of high-intensity focused ultrasound (HIFU) procedures (a) and at 17 weeks' gestation, after final HIFU procedure (b).

The patient did not exhibit any signs or symptoms of threatened premature labor, such as uterine contractions or dilation of the cervix, either during or following the procedure. Furthermore, the pump fetus did not exhibit any abnormal behavior and its heart rate and umbilical blood flow did not vary. However, at 28 weeks' gestation the fetus appeared small for gestational age, indicating fetal growth restriction. At 37 weeks' gestation, an emergency Cesarean section was performed owing to a rapid increase in the patient's blood pressure (170/100 mmHg). A male neonate was born weighing 1903 g with Apgar scores of 8 and 9 at 1 and 5 min, respectively. We performed the auditory brainstem response test, which confirmed that the auditory function of the neonate was intact. Congenital pseudarthrosis of the left leg was later diagnosed by an orthopedist, but other than this the neonate was healthy and was discharged without any other abnormalities.

The length of the acardiac fetus was 5.5 cm (Figure 3). It had a shrunken and macerated appearance with tissue degeneration. The cord was not visible at the time of delivery, so we could not obtain macroscopic or histological findings of the site targeted by HIFU irradiation.

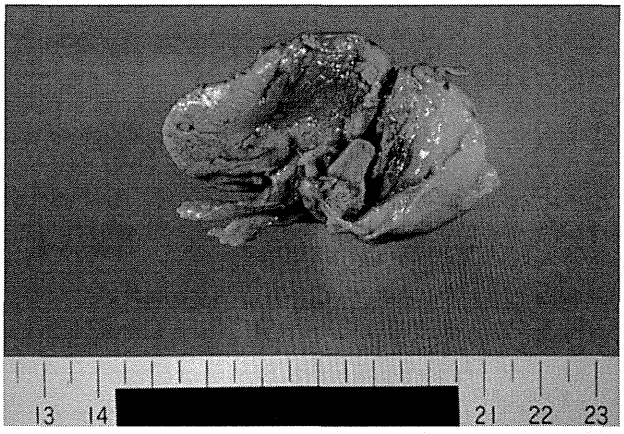

Figure 3 Postdelivery photograph of acardiac fetus.

DISCUSSION

This is the first case in which HIFU treatment has been successfully conducted on a human fetus. Through previously conducted animal experiments[2,3], we identified TRAP sequence as the most suitable fetal disorder for *in-utero* treatment with HIFU.

Recently, TRAP sequence has been treated using radiofrequency ablation therapy[4,5], which is less invasive than the endoscopic technique that has been applied in the past[6,7]. However, because of the insertion of devices into the uterus, the radiofrequency ablation procedure is associated with a risk of hemorrhage, rupture of membranes and premature birth. In contrast, HIFU treatment is a non-invasive procedure that uses external ultrasound waves that can be transmitted through solid tissue and focused within the body to destroy deep target tissues. It has been proven through animal experiments that HIFU enables thermal denaturation of fetal blood vessels without direct fetal contact[3].

Irradiation treatment with HIFU at 13 weeks' gestation did not increase the temperature of the fetal blood vessel wall adequately to accomplish occlusion of blood flow. This result was probably due to inadequate ultrasound intensity at the focal point. In previous animal experiments, adequate ultrasound intensity at the focal point was obtained when the transducer output was 100 W with 83% transfer efficiency[3]. However the same intensity would not have been achieved in a human patient owing to attenuation of ultrasound power that would occur as it passes through the subcutaneous fat layer, which is thinner in experimental animals. Therefore, we increased the emitting electrical power to 200 W, as previously tested in animal experiments, in which a greater ultrasound intensity had been successfully obtained. The intensity at the focal point was theoretically 4600 W/cm^2 without considering any attenuation, achieving complete occlusion of blood flow in the acardiac fetus. Following this successful experience, we will consider higher HIFU intensities at the initial irradiation treatment in future cases.

Compared with conventional therapy for TRAP sequence, the advantage of HIFU is that it does not cause injury to the mother or the uterus, except after a long irradiation time. In this instance, the patient experienced abdominal warmth and lower back pain when the focused and widened HIFU beam hit the lumbar vertebrae. Therefore, as long as we can control levels of abdominal warmth and the direction of the ultrasound beam, we can treat TRAP sequence non-invasively by HIFU.

It is difficult to determine whether HIFU exposure was associated with the neonate's pseudarthrosis of the leg. Although in this case the cause of this disease is unknown, there is a well-known relationship between congenital pseudarthrosis and neurofibramotosis type 1, an autosomal dominant disease[8]. In this case, there were no other affected individuals in the family. We think it is likely that the condition arose spontaneously, because the acoustic window did not include the pump fetus; that is, the HIFU beam did not pass through the pump fetus, including the left limb. We also do not believe that there is any association between the HIFU procedure and the occurrence of pregnancy-induced hypertension and fetal growth restriction seen in this case because placental pathology revealed no sign of the typical lesions often induced by HIFU exposure, and the HIFU beam did not pass through the placenta. At last follow-up the neonate was healthy, excluding pseudarthrosis of the left leg. However, long-term neurodevelopmental outcome after fetal therapy cannot yet be assessed[9], therefore further follow-up of this case over a long period of time is necessary.

The present case adds a new possible modality for non-invasive *in-utero* treatment of TRAP sequence.

REFERENCES

1. Ichizuka K, Hasegawa J, Nakamura M, Matsuoka R, Sekizawa A, Okai T, Umemura S. High-intensity focused ultrasound treatment for twin reversed arterial perfusion sequence. *Ultrasound Obstet Gynecol* 2012; 40: 476–478.
2. Ishikawa T, Okai T, Sasaki K, Umemura S, Fujiwara R, Kushima M, Ichihara M, Ichizuka K. Functional and histological changes in rat femoral arteries by HIFU exposure. *Ultrasound Med Biol* 2003; 29: 1471–1477.
3. Ichizuka K, Ando S, Ichihara M, Ishikawa T, Uchiyama N, Sasaki K, Umemura S, Matsuoka R, Sekizawa A, Okai T. Application of high-intensity focused ultrasound for umbilical artery occlusion in a rabbit model. *Ultrasound Obstet Gynecol* 2007; 30: 47–51.
4. Tsao K, Feldstein VA, Albanese CT, Sandberg PL, Lee H, Harrison MR, Farmer DL. Selective reduction of acardiac twin by radiofrequency ablation. *Am J Obstet Gynecol* 2002; 187: 635–640.
5. Bebbington MW, Danzer E, Moldenhauer J, Khalek N, Johnson MP. Radiofrequency ablation vs bipolar umbilical cord coagulation in the management of complex monochorionic pregnancies. *Ultrasound Obstet Gynecol* 2012; 40: 319–324.
6. Hecher K, Lewi L, Gratacos E, Huber A, Ville Y, Deprest J. Twin reversed arterial perfusion: fetoscopic laser coagulation of placental anastomoses or the umbilical cord. *Ultrasound Obstet Gynecol* 2006; 28: 688–691.
7. Nakata M, Sumie M, Murata S, Miwa I, Matsubara M, Sugino N. Fetoscopic laser photocoagulation of placental communicating vessels for twin-reversed arterial perfusion sequence. *J Obstet Gynaecol Res* 2008; 34: 649–652.
8. Pannier S. Congenital pseudarthrosis of the tibia. *Orthop Traumatol Surg Res* 2011; 97: 750–761.
9. van Klink JM, Koopman HM, Oepkes D, Walther FJ, Lopriore E. Long-term neurodevelopmental outcome in monochorionic twins after fetal therapy. *Early Hum Dev* 2011; 87: 601–606.

Relative Residence Time Prolongation in Intracranial Aneurysms: A Possible Association With Atherosclerosis

Shin-ichiro Sugiyama, MD*‡
Kuniyasu Niizuma, MD*
Toshio Nakayama, PhD§
Hiroaki Shimizu, MD¶
Hidenori Endo, MD¶
Takashi Inoue, MD¶
Miki Fujimura, MD||
Makoto Ohta, PhD#
Akira Takahashi, MD§
Teiji Tominaga, MD*

*Department of Neurosurgery, Tohoku University Graduate School of Medicine, Sendai, Japan; ‡Department of Neuroanesthesia, and ¶Department of Neurosurgery, Kohnan Hospital, Sendai, Japan; §Graduate School of Biomedical Engineering, and #Institute of Fluid Science, Tohoku University, Sendai, Japan; ||Department of Neurosurgery, Sendai Medical Center, Sendai, Japan

Correspondence:
Kuniyasu Niizuma, MD, PhD,
Department of Neurosurgery,
Tohoku University
Graduate School of Medicine,
1-1 Seiryo-machi, Aoba-ku, Sendai,
Miyagi 980-8574, Japan.
E-mail: niizuma@nsg.med.tohoku.ac.jp

Received, September 27, 2012.
Accepted, July 10, 2013.
Published Online, July 16, 2013.

WHAT IS THIS BOX?
A QR Code is a matrix barcode readable by QR scanners, mobile phones with cameras, and smartphones. **The QR Code above links to Supplemental Digital Content from this article.**

BACKGROUND: Intracranial aneurysms can have atherosclerotic wall properties that may be important in predicting aneurysm history or estimating the potential risks of surgical treatments.
OBJECTIVE: To investigate hemodynamic characteristics of atherosclerotic lesions in intracranial aneurysms using computational fluid dynamics.
METHODS: Intraoperative video recordings of 30 consecutive patients with an unruptured middle cerebral artery aneurysm were examined to identify atherosclerotic lesions on an aneurysm wall. For computational fluid dynamics analyses, geometries of aneurysms and adjacent arteries were reconstructed from 3-dimensional rotational angiography. Transient simulations were conducted under patient-specific pulsatile inlet conditions measured by phase-contrast magnetic resonance velocimetry. Three hemodynamic wall parameters were calculated: time-averaged wall shear stress, oscillatory shear index, and relative residence time (RRT). Statistical analyses were performed to discriminate the risk factors of atherosclerotic lesion formation.
RESULTS: Among 30 aneurysms, 7 atherosclerotic lesions with remarkable yellow lipid deposition were identified in 5 aneurysms. All 7 atherosclerotic lesions spatially agreed with the area with prolonged RRT. Univariate analysis revealed that male sex ($P = .03$), cigarette smoking ($P = .047$), and maximum RRT ($P = .02$) are significantly related to atherosclerotic lesion on the intracranial aneurysmal wall. Of those variables that influenced atherosclerotic lesion of the intracranial aneurysmal wall, male sex ($P = .005$) and maximum RRT ($P = .004$) remained significant in the multivariate regression model.
CONCLUSION: The area with prolonged RRT colocalized with atherosclerotic change on the aneurysm wall. Male sex and maximum RRT were independent risk factors for atherogenesis in intracranial aneurysms.

KEY WORDS: Atherosclerosis, Cerebral aneurysm, Hemodynamics, Oscillatory shear stress, Relative residence time, Wall shear stress

Neurosurgery 73:767–776, 2013 DOI: 10.1227/NEU.0000000000000096 www.neurosurgery-online.com

With recent advances in diagnostic neuroradiological imaging, many unruptured intracranial aneurysms have been discovered. Several large prospective studies showed that some morphological factors such as size, location, and irregular shape might help to predict the risk for rupture of unruptured aneurysms.[1,2] However, biomechanical reasons underlying these morphological risk factors remain unclear. The morphology of an aneurysm has a definite influence on the hemodynamics inside that aneurysm. Therefore, recent studies have investigated the relation between aneurysm geometry and hemodynamics and the role of this relation in the natural history of intracranial aneurysms.[3,4]

ABBREVIATIONS: CFD, computational fluid dynamics; **MCA,** middle cerebral artery; **OSI,** oscillatory shear index; **RRT,** relative residence time; **WSS,** wall shear stress

Supplemental digital content is available for this article. Direct URL citations appear in the printed text and are provided in the HTML and PDF versions of this article on the journal's Web site (www.neurosurgery-online.com).

Progress in computational fluid dynamics (CFD) has enabled hemodynamic simulation in realistic aneurysm geometries with increased accuracy and reliability.[5] In postvisualization of CFD simulation, blood flow inside aneurysms can be demonstrated using streamlines or velocity vector plots. In addition, the influence of intra-aneurysmal blood flow on the vascular wall can be characterized by hemodynamic wall parameters that are calculated from the results of CFD such as wall shear stress (WSS) and the oscillatory shear index (OSI). WSS is the tangential frictional stress caused by blood flow on the vascular wall. OSI is a dimensionless measure of directional changes in WSS and is used as a marker of the oscillatory nature of WSS.

These hemodynamic wall parameters are related to the biological processes on the aneurysm wall, and CFD simulations may be able to predict the rupture of intracranial aneurysms.[4,6-8] In particular, low WSS and high OSI have been proposed as indicators for the risk of aneurysm rupture.[4] Blood flow associated with such low or oscillatory WSS is generically considered a kind of disturbed blood flow,[9,10] although disturbed flow has many definitions. Aneurysm rupture may be driven by biological processes mediated by unphysiological WSS conditions, which have been shown to activate proinflammatory signaling pathways in endothelial cells.[11] Activation of such inflammatory pathways might cause degradation of the aneurysm wall and rupture of the aneurysms.[12,13]

On the other hand, low or oscillatory WSS is known to be a potential atherogenic stimulus in large arteries.[7,10,14] We previously reported a hemodynamic study of an intracranial aneurysm with atherosclerotic blebs that were subjected to low and oscillatory WSS.[15] These results suggest that such blood flow may have the potential to promote atherogenesis in intracranial aneurysms and in large arteries. Therefore, low or oscillatory WSS might cause different consequences, including rupture and atherogenesis. However, the mechanism or what triggers these different consequences is unknown. In particular, little work has been done on the atherosclerotic lesions of the intracranial aneurysms. The purpose of this study is to investigate the roles of hemodynamics on atherosclerosis in intracranial aneurysms. This knowledge may be important for estimating potential risks of surgery or in predicting the natural history of intracranial aneurysms.

We conducted CFD analysis of unruptured middle cerebral artery (MCA) aneurysms that were surgically treated and investigated the relation between the spatial distribution of atherosclerotic lesions on the aneurysm wall and hemodynamic wall parameters, including WSS and OSI. In addition to WSS and OSI, we calculated the relative residence time (RRT) introduced by Himburg et al[9] as a marker of low or oscillatory WSS. We also investigated intra-aneurysmal flow fields, which may be responsible for atherosclerosis in intracranial aneurysms.

PATIENTS AND METHODS

Patient Population

From October 2010 to September 2011, 30 unruptured MCA aneurysms were surgically treated at our hospital. All patients underwent 3-dimensional (3-D) rotational angiography and magnetic resonance (MR) examination, including velocity measurement of parent arteries, before the surgical treatment. Intraoperative video recordings were examined to distinguish atherosclerotic lesions on the aneurysm wall. This study was conducted in accordance with and under the approval of the ethics review board of our hospital.

Model Construction

Conventional digital subtraction and 3-D rotational angiography was performed by standard transfemoral catheterization with a biplane unit (Innova 3131; GE Healthcare Japan, Tokyo, Japan). These images were obtained during a 6-second injection of a contrast agent and a 200° rotation with imaging at 30 frames per second for 5 seconds. The 150 projection images were reconstructed into a 3-D data set of $512 \times 512 \times 512$ isotropic voxels covering a field of view of 200 mm in all 3 directions.

The 3-D data set obtained from rotational angiography was exported to a personal computer to form a 3-D isosurface model of the aneurysms. The mean signal intensity of the parent artery (M1) was calculated and used as an initial threshold. A 3-D surface was extracted with the threshold using imaging software (Avizo 6.2; Visualization Science Group, Merignac, France). It was then displayed on the native axial, coronal, and sagittal slices of the original 3-D data set and adjusted until it visually matched the luminal boundary of all regions of interest. The results of segmentation were validated by 2-dimensional conventional angiograms in the anteroposterior and lateral views and intraoperative videograms of vessels and aneurysms exposed during surgery. The segmented 3-D surface was then processed with commercial software (Magics RP 13.1; Materialise, Leuven, Belgium) to smooth the fine irregularities, to make planes for inlets and outlets, and to clear small branches from the regions of interest. The rate of volume change was suppressed to $\leq$ 5% during the smoothing process. The data were output in a stereolithography format.

Quantitative MR Velocimetry

Quantitative MR velocimetry was performed with a 3-T MR image scanner (Signa HDxt; GE Healthcare Japan, Tokyo, Japan) before the surgical treatment. The protocol entails a standard cranial 3-D time-of-flight MR angiography to select a slice orientation for the arterial blood flow measurements. The optimal perpendicular scan plane was determined from the acquired time-of-flight images. The coordinates obtained specified the position of an oblique fast 2-dimensional phase-contrast sequence that was then performed on the basis of these coordinates using a peripheral gated 2-dimensional phase-contrast sequence with the following imaging parameters: repetition time/echo time/number of excitations, 25 milliseconds/5.4 milliseconds/1; field of view, 160×160 mm; matrix, 512×512; voxel size, 0.3×0.3 mm; velocity encoding, 100 cm/s; imaging time, about 5 minutes; direction, transaxial; peripheral gated with ECG; and phases, 30. The acquired phase-contrast images were transferred to the workstation for flow quantification with dedicated software (CV Flow; GE Healthcare Japan). A region of interest was placed semiautomatically on the phase-contrast images over a cardiac cycle. The velocities at all of the pixels inside the vessel border were integrated to calculate the flow in milliliters per second, and these values were used to obtain the quantitative waveform over the cardiac cycle (Figure 1).

Numerical Simulations

Each aneurysm model was meshed with the use of commercial software (ICEM CFD; ANSYS Inc, Lebanon, New Hampshire) to create tetrahedral meshes with 3 layers of finer-prism meshes in the boundary,

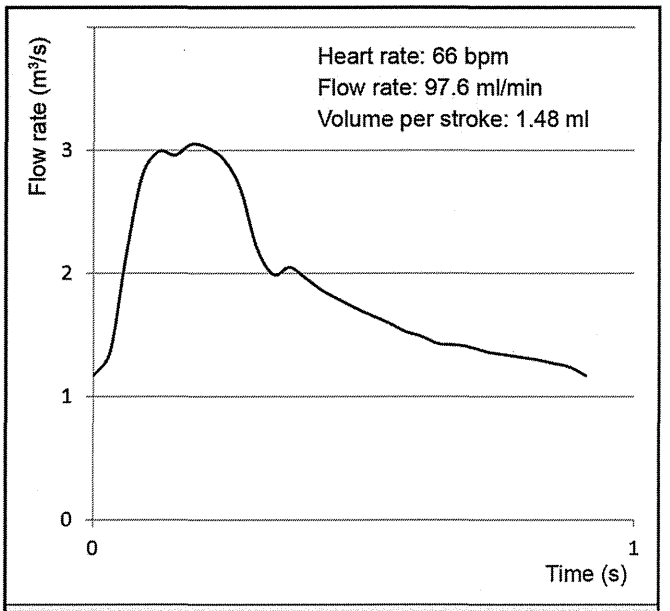

FIGURE 1. *An example of pulsatile waveform, heart rate, mean flow rate, and flow volume per stroke obtained from phase-contrast magnetic resonance velocimetry (case 2).*

resulting in approximately 1 million meshes. A finite-volume method package, ANSYS 12.1 (ANSYS Inc), was used to solve the governing equations: 3-D unsteady Navier-Stokes equations and equation of continuity. The patient-specific pulsatile-flow condition derived from the MR examinations was prescribed at the inlet boundary. The diffusion fluxes in the direction normal to the inlet plane were assumed to be zero, and normal gradients were neglected. Traction-free conditions (0 Pa) were substituted for outlets. Following the conventions for CFD in large vessels,[16] blood was modeled as an incompressible newtonian fluid with a density of 1050 kg/m^3 and a viscosity of 0.0035 kg/m·s. A rigid-wall no-slip boundary condition was implemented at the vessel walls. Three pulsatile cycles were simulated to ensure that numeric stability was reached, and the results from the third cycle were used for analysis.

Data Analysis

Three hemodynamic wall parameters including WSS, OSI, and RRT were calculated. Time-averaged WSS refers to the tangential frictional stress caused by the action of blood flow on the vessel wall. OSI is a dimensionless measure of directional changes in WSS to describe the temporal disturbance of intra-aneurysmal flow.[17] RRT demonstrates the residence time of particles near the wall, and RRT prolongation corresponds with low or oscillatory WSS.[9] These data were used to investigate the relation between the 3 parameters and atherosclerotic change of the aneurysms. Moreover, the maximum RRT, maximum OSI, and minimum WSS of each aneurysm were used for statistical analysis to find predictors of atherosclerosis in intracranial aneurysms. To visualize the flow field, 3-D streamlines of intra-aneurysmal flow and WSS vectors on the aneurysm wall over a cardiac cycle were plotted in the model with the use of commercial software (ANSYS CFD; Ansys Inc). Supplemental Digital Content 1 (http://links.lww.com/NEU/A577) gives a detailed description of WSS, OSI, and RRT.

An unpaired *t* test was used for parametric statistical analysis. Categorical variables were analyzed in contingency tables with the Fisher exact test. Results with values of $P < .05$ were considered statistically significant. In a second step, a multivariate analysis was performed to find independent predictors for the atherosclerotic lesions of the aneurysmal wall using a binary logistic regression analysis and to find confounding factors between potentially independent predictors. Variables with significant *P* values in univariate analyses were considered potentially independent variables in the multivariate analysis. A forward stepwise method was used to construct multivariate logistic regression models with the inclusion criterion of $P < .05$. All calculations were performed with standard commercial software (JMP Pro Version 9.02; SAS Institute Inc).

RESULTS

Intraoperative video recordings were examined for all 30 cases. The profiles of patients are listed in Table 1. Seven atherosclerotic lesions on 5 aneurysms (5 of 30, 16.7%) were distinguished by remarkable yellow lipid deposition. Five atherosclerotic lesions were located on the aneurysm dome, and 2 were located at the bleb. All 5 patients had several vascular atherosclerosis risk factors such as male sex, old age, obesity, smoking history, hypertension, diabetes mellitus, or dyslipidemia. MR velocimetry successfully measured the flow rate and flow volume per stroke of each patient (Figure 1). MR imaging indicated no thrombus in the aneurysms of all patients.

Among the 3 hemodynamic variables examined in the present study, only RRT demonstrated qualitative agreement with the spatial distribution of atherosclerosis in all 7 lesions as a single metric (Figures 2-4). All atherosclerotic lesions presented with high RRT and low WSS. The 5 lesions on the dome were exposed to low and oscillatory WSS at the center of vortex flow (cases 1-3; Figures 2 and 3). In these 5 lesions, the RRT was concentric circular from the center of vortex, and the highest RRT and OSI and lowest WSS were observed at the same point at the vortex center. On the other hand, the 2 lesions at the bleb were subjected to low WSS induced by flow expansion at the bleb (cases 4 and 5; Figure 4). In these 2 regions, the site with the maximum RRT was different from both the site with maximum OSI and the site with minimum WSS. In contrast, RRT was not markedly prolonged in aneurysms without atherosclerotic lesions.

To evaluate the risk factor of atherosclerotic change of the intracranial aneurysms, statistical analyses were performed (Table 2). Univariate analysis revealed that male sex ($P = .03$), cigarette smoking ($P = .047$), and maximum RRT ($P = .02$) are significantly related to atherosclerotic lesion on the intracranial aneurysmal wall. Of those variables that influenced atherosclerotic lesion of the intracranial aneurysmal wall, the variable male ($P = .005$) and maximum RRT ($P = .004$) remained significant in the multivariate regression model ($R^2 = 0.52$). Cigarette smoking was not chosen by the forward stepwise method. In the multivariate regression model, the variables that were not significant in the univariate analyses were eliminated.

TABLE 1. Clinical Characteristics of Patients With a Middle Cerebral Artery Aneurysm

Case	Sex, Age, y	Aneurysm Size, mm	Atherosclerotic Lesions, n	Body Mass Index, kg/m^2	Cigarette Smoking	Hypertension	Diabetes Mellitus	Dyslipidemia
1	M, 57	4.1	1	22.7	+	+	+	−
2	F, 76	7.2	2	20.9	−	−	−	+
3	M, 64	6.4	2	25.0	+	+	−	−
4	M, 53	6.1	1	27.1	+	+	−	−
5	M, 66	9.0	1	22.4	+	+	−	−
6	F, 64	6.9	0	22.7	−	+	−	+
7	F, 50	5.0	0	21.8	−	−	−	−
8	M, 32	4.6	0	30.6	−	+	−	−
9	F, 57	6.0	0	19.4	+	−	−	−
10	M, 64	5.6	0	24.2	−	+	−	−
11	M, 43	4.5	0	28.3	−	−	−	−
12	M, 63	5.9	0	21.3	+	−	−	−
13	F, 68	6.1	0	23.1	−	−	−	−
14	F, 60	7.9	0	19.2	−	−	−	−
15	F, 70	5.2	0	23.4	−	−	−	−
16	M, 64	4.7	0	27.6	+	+	+	+
17	F, 63	6.1	0	23.8	+	−	−	+
18	F, 56	4.1	0	30.9	−	+	+	+
19	F, 52	4.6	0	27.8	−	+	−	−
20	F, 62	5.3	0	32.9	−	+	−	+
21	F, 44	3.5	0	23.3	+	+	−	−
22	F, 56	4.6	0	22.9	−	−	−	−
23	M, 65	5.4	0	25.3	+	+	+	+
24	F, 65	5.1	0	19.1	−	−	−	+
25	F, 55	11.3	0	21.7	+	−	−	−
26	F, 63	6.0	0	20.4	−	+	−	−
27	F, 54	4.0	0	21.1	−	−	−	−
28	F, 74	7.9	0	22.7	−	+	−	+
29	F, 68	7.7	0	24.0	−	−	−	−
30	F, 66	6.0	0	23.4	−	+	−	+

Illustrative Cases

Case 1

A hypertensive 57-year-old man with an unruptured right MCA aneurysm of 4.1-mm maximum diameter underwent open surgery 3 months after an angiographic examination. The heterogeneous aneurysm wall with partial atherosclerosis was confirmed intraoperatively (Figure 2A). The atherosclerotic lesion of the aneurysm was subjected to disturbed blood flow indicated by prolongation of the RRT (maximum RRT = 36.1; Figure 2B). The area with prolonged RRT also had low WSS and high OSI (minimum WSS = 0.053 Pa, maximum OSI = 0.24; Figure 2B-2D). Snapshots of WSS vector plots captured at end diastole and peak systole revealed that WSS vectors were arranged in a whirl-like fashion around the vortex center, which moved around over pulsatile cycle (Figure 2E and 2F; white squares). Snapshots of the flow field (3-D streamlines) captured at end diastole and peak systole revealed an intra-aneurysmal vortex flow that moved around over pulsatile cycle and caused high OSI in the corresponding area (Figure 2G and 2H). In summary, in this case, the vortex flow induced local disturbed flow with low and oscillatory WSS, in accordance with the atherosclerotic lesion.

Case 2

A 76-year-old woman presented with subarachnoid hemorrhage. Catheter angiography revealed 4 intracranial aneurysms. Two months after the first clipping surgery of the ruptured left MCA aneurysm, an unruptured right MCA aneurysm of 7.2-mm maximum diameter was also clipped. This unruptured aneurysm had 2 yellowish atherosclerotic lesions (Figure 3A and 3B). Both atherosclerotic lesions were subjected to disturbed blood flow indicated by prolongation of the RRT (maximum RRT = 27.4 and 16.4; Figure 3C and 3D). Both areas with prolonged RRT presented high OSI (maximum OSI = 0.35 and 0.30; Figure 3E and 3F) and low WSS (minimum WSS = 0.12 and 0.15 Pa; Figure 3G and 3H). Snapshots of WSS vector plots captured at end diastole and peak systole revealed that WSS vectors were arranged in a whirl-like fashion around the vortex center (data not shown).

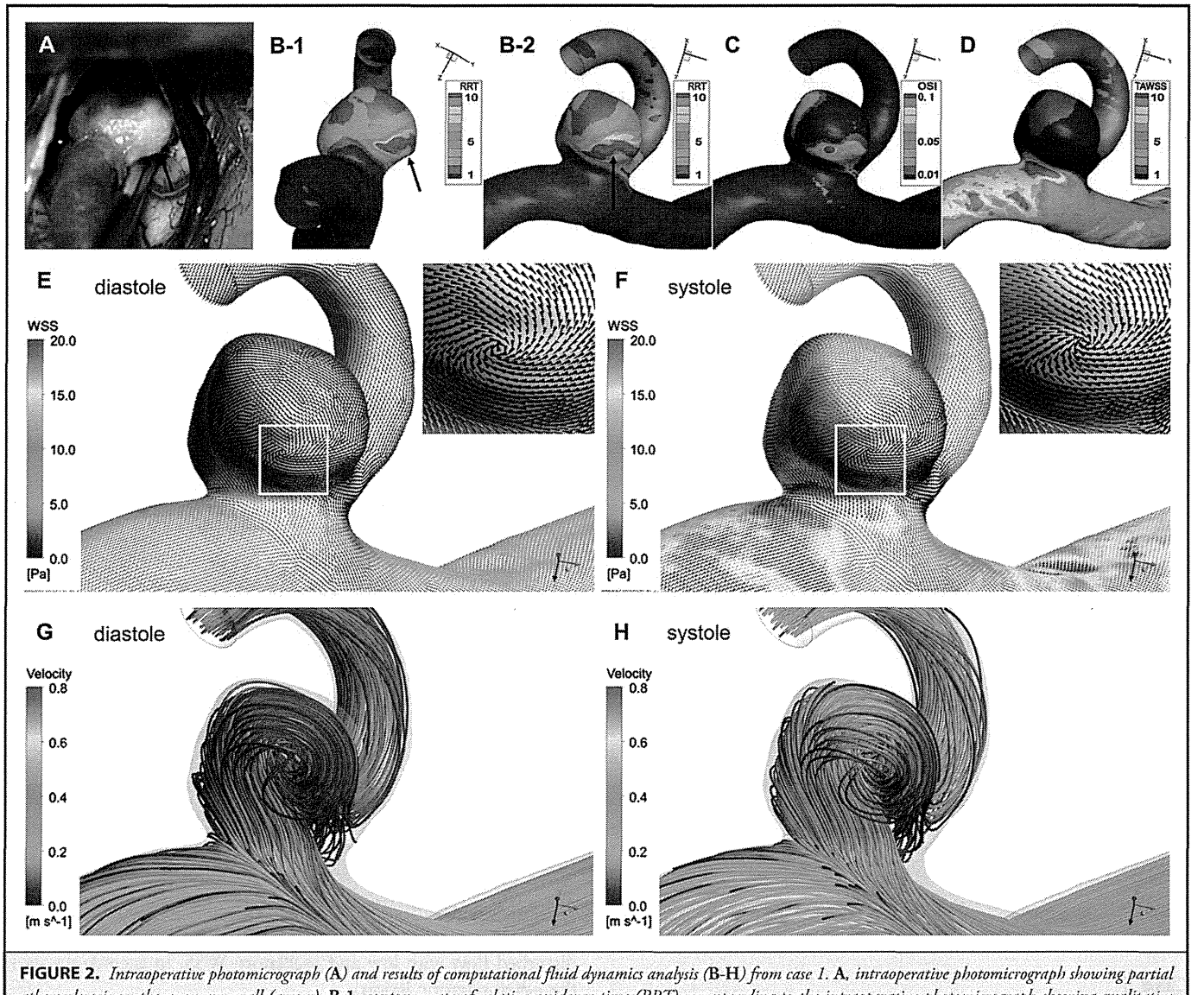

FIGURE 2. *Intraoperative photomicrograph* (**A**) *and results of computational fluid dynamics analysis* (**B-H**) *from case 1.* **A**, *intraoperative photomicrograph showing partial atherosclerosis on the aneurysm wall (arrow).* **B-1**, *contour maps of relative residence time (RRT) corresponding to the intraoperative photomicrograph showing qualitative agreement of the prolonged RRT (arrows) with the spatial distribution of atherosclerosis shown in* **A**. *RRT* (**B-2**), *oscillatory shear index (OSI;* **C**), *and time-averaged wall shear stress (WSS;* **D**) *from the same viewing angle indicate that the distribution of the area with prolonged RRT presents a high OSI value and low WSS magnitude. Snapshots of WSS vector plots captured at end diastole* (**E**) *and peak systole* (**F**) *reveal that WSS vectors are arranged in a whirl-like fashion around the vortex center* (**E** *and* **F**; *white squares). Snapshots of the flow field (3-dimensional streamlines) captured at end diastole* (**G**) *and peak systole* (**H**) *show slow and vortex flow. Maximum RRT is 36.1* (**B-1** *and* **B-2**, *arrows) and is localized at the same point as maximum OSI (0.24) and minimum WSS (0.053 Pa).*

Snapshots of the flow fields (3-D streamlines) captured at end diastole and peak systole revealed intra-aneurysmal vortices that were slow and oscillatory, in accordance with the atherosclerotic lesions of the aneurysm (data not shown).

Case 5

A 66-year-old man presented with an unruptured right MCA aneurysm of 4.0-mm maximum diameter that enlarged to a diameter of 9.0 mm 3 years after the initial MR angiography. This aneurysm had 3 blebs: 1 bleb had a yellowish atherosclerotic wall, but the other 2 blebs had reddish and rather thin walls (Figure 4A). The atherosclerotic bleb was subjected to disturbed blood flow indicated by prolongation of the RRT (Figure 4B). The area with prolonged RRT presented with low WSS but mild elevation of OSI (Figure 4B-4D). Snapshots of WSS vector plots captured at end diastole and peak systole revealed that WSS vectors were not arranged in a whirl-like fashion (Figure 4E and 4F). Snapshots of the flow field

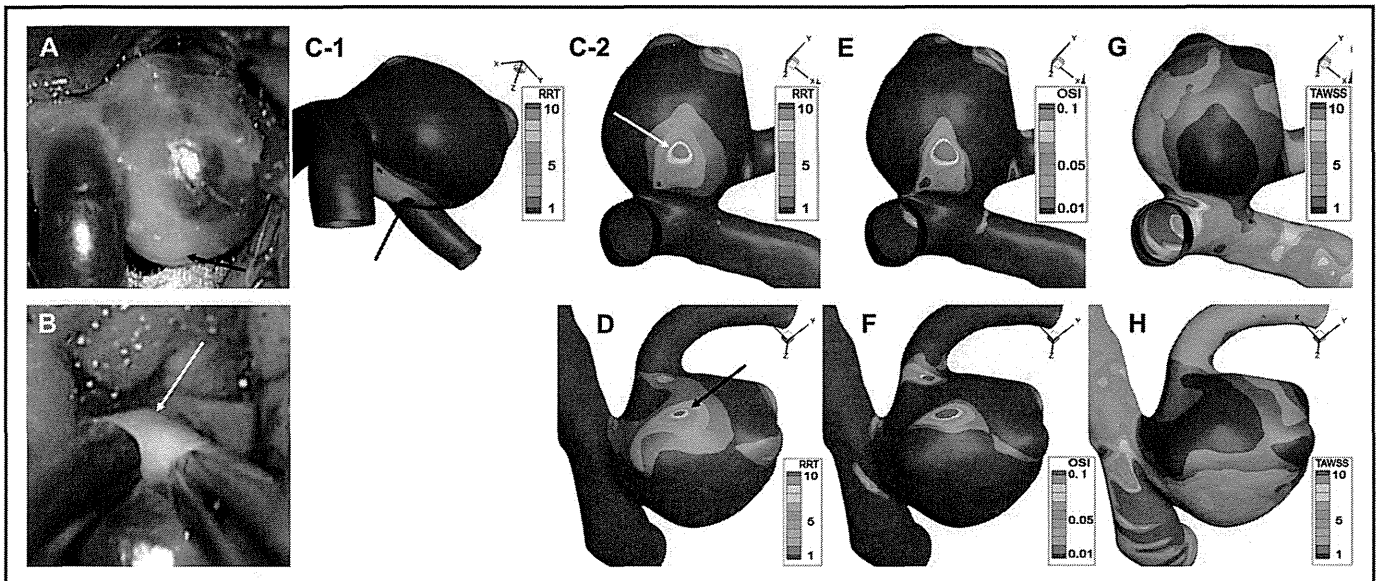

FIGURE 3. *Intraoperative photomicrograph (A and B) and results of computational fluid dynamics analysis of an atherosclerotic lesion (C-H) from case 2. Intraoperative photomicrograph shows 2 partial atherosclerotic lesions on the aneurysm wall (A and B, arrows). C, E, and G, view angle to observe the atherosclerotic lesion shown in A; D through F, view angle for the lesion shown in B. C and D, contour maps of relative residence time (RRT) indicate qualitative agreement of the prolonged RRT (arrows) with the spatial distribution of atherosclerosis shown in A and B. Oscillatory shear index (OSI; E and F) and time-averaged wall shear stress (WSS; G and H) indicate that the area with prolonged RRT also has high OSI and low WSS. Maximum RRT is 27.4 (C) and 16.4 (D). The corresponding OSI is 0.35 (E) and 0.30 (F). The corresponding WSS is 0.12 Pa (G) and 0.15 Pa (H).*

(3-D streamlines) captured at end diastole (Figure 4G) and peak systole (Figure 4H) revealed excessive slow flow, even at peak systole, that resulted from flow expansion at the bleb (Figure 4H). In summary, the atherosclerotic bleb had prolongation of RRT, accompanied not by vortex but by flow expansion at the bleb. Maximum RRT was 29.7 and the corresponding OSI and WSS were 0.03 and 0.15 Pa, respectively (Figure 4B-4D). The site with the maximum RRT was different from both the site with the maximum OSI and the site with the minimum WSS.

Case 27

A 54-year-old woman with an unruptured right MCA aneurysm of 4.0-mm maximum diameter underwent open surgery. Although this aneurysm had no atherosclerotic lesion, intraoperative video recording revealed heterogeneous wall properties: reddish translucent wall with whitish thick-walled patches (Figure 5A). The RRT was not markedly prolonged on the aneurysm. Interestingly, the area with maximum RRT (RRT = 6.6; Figure 5B), which had minimum WSS and maximum OSI (WSS = 0.28 Pa, OSI = 0.23; Figure 5C and 5D), corresponded to the whitish thick wall. It was located at the center of the tiny intra-aneurysmal vortex, which was shown by WSS vector plots and 3-D streamlines (Figure 5E-5H). In summary, in this case, a slight increase in RRT was seen at the center of the tiny intra-aneurysmal vortex, in accordance with the whitish thick wall, although the aneurysm had no atherosclerotic lesions.

DISCUSSION

To the best of our knowledge, this is the first report investigating hemodynamic characteristics of atherosclerotic lesions in intracranial aneurysms. From 30 MCA aneurysms investigated in this study, 7 atherosclerotic lesions on 5 aneurysms were identified. All 5 patients with an atherosclerotic aneurysm had several vascular atherosclerosis risk factors. Among these vascular risk factors, male sex remained an independent risk factor of the atherosclerotic aneurysmal wall lesion of the intracranial aneurysms. Although cigarette smoking did not remain significant in the multivariate analysis, it was significant in the univariate analysis and may also be important. Results of hemodynamic simulations using patient-derived inlet conditions showed that all 7 atherosclerotic lesions colocalized with the area with prolonged RRT. In contrast, aneurysms without prolonged RRT had no atherosclerotic lesions. The flow rate in each patient measured by quantitative MR velocimetry was compatible with previous data reported by Zhao et al.[18] Statistical analyses also revealed that prolongation of maximum RRT is an independent risk factor of the atherosclerotic aneurysmal wall lesion of the intracranial aneurysms.

Himburg et al[9] proposed RRT as a robust marker of disturbed blood flow with low or oscillatory WSS. From the mathematical definition of RRT, its prolongation is characterized by 2 properties: low velocity with low WSS and oscillatory behavior with high OSI. Notably, OSI is insensitive to WSS

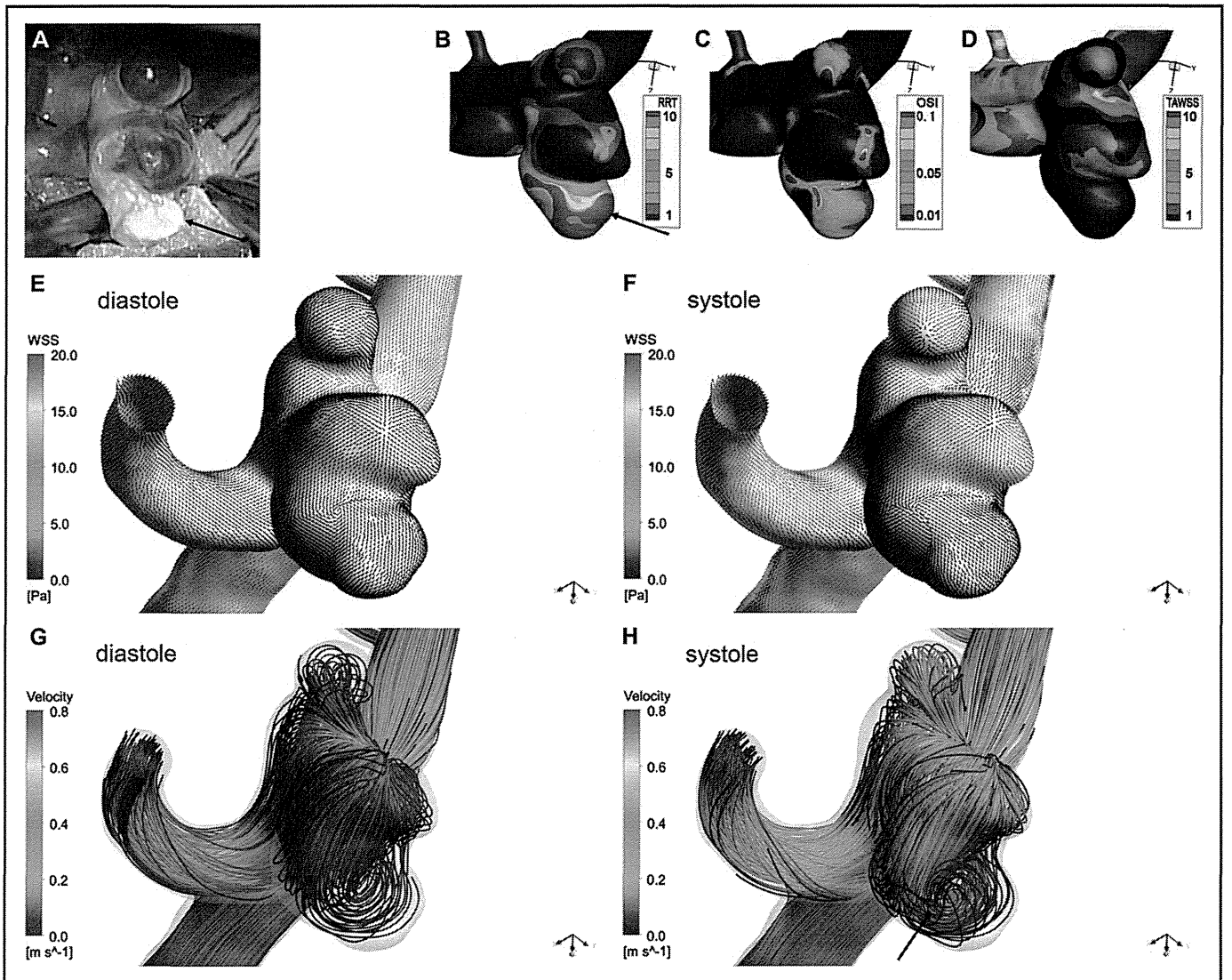

FIGURE 4. *Intraoperative photomicrograph* (**A**) *and results of computational fluid dynamics analysis of an atherosclerotic lesion* (**B-H**) *from case 5.* **A**, *intraoperative photomicrograph showing partial atherosclerosis on the aneurysm wall (arrow).* **B**, *a contour map of relative residence time (RRT) indicating qualitative agreement of the prolonged RRT (arrow) with the spatial distribution of atherosclerosis shown in* **A**. *RRT* (**B**), *oscillatory shear index (OSI;* **C**), *and time-averaged wall shear stress (WSS;* **D**) *from the same viewing angle indicate that the area with prolonged RRT has medium OSI and low WSS. Snapshots of WSS vector plots captured at end diastole* (**E**) *and peak systole* (**F**) *reveal that WSS vectors are not arranged in a whirl-like fashion. Snapshots of the flow field (3-dimensional streamlines) captured at end diastole* (**G**) *and peak systole* (**H**) *demonstrate extremely slow flow even at peak systole* (**H**). *Vortex flow is visualized near the bleb at peak systole* (**H**, *arrow), but RRT prolongation in this case results from the expansion of inflow to the bleb. Maximum RRT is 29.7* (**B**, *arrow). The corresponding OSI and WSS are 0.03 and 0.15 Pa, respectively. The site with maximum RRT is different from both the site with the maximum OSI and the site with the minimum WSS.*

magnitude, and sites with low WSS may be, but are not necessarily, sites of high OSI. Low WSS can result from flow expansion without any local flow oscillation.[9] In our study, the prolongation of RRT by an intra-aneurysmal vortex occurred with low and oscillatory WSS, whereas RRT prolongation by flow expansion at the bleb occurred with low but not oscillatory WSS. Regardless of the OSI variation, RRT could be used as a single metric for identifying atherosclerotic lesions.

This study consists of a small number of materials and lacks sequential observation with time. Therefore, results of this study can only propound a possible relation between RRT and atherogenesis on an aneurysm wall and cannot provide evidence for a causal relation. However, biomechanical links between disturbed flow and atherosclerosis are well established. Hemodynamic conditions with low and oscillatory WSS activate atherogenic and proinflammatory signaling pathways in endothelial

TABLE 2. Risk Factors for Atherosclerosis on the Cerebral Aneurysmal Wall[a]

	Sex	Mean ± SD Age, y	Mean ± SD Aneurysm Size, mm	Mean ± SD Body Mass Index, kg/m^2	Cigarette Smoking, n (%)	Hypertension, n (%)	Diabetes Mellitus, n (%)	Dyslipidemia, n (%)	Maximum ± SD RRT	Maximum ± SD OSI	Minimum ± SD WSS, Pa
Patients with atherosclerotic aneurysms (n = 5)	M/F: 4/1 (M: 80)	63.2 ± 8.9	6.6 ± 1.8	23.6 ± 2.4	4 (80)	4 (80)	1 (20)	1 (20)	21.7 ± 13.3	0.20 ± 0.12	0.15 ± 0.07
Patients without atherosclerotic aneurysms (n = 25)	M/F: 6/19 (M: 24)	59.1 ± 9.5	5.8 ± 1.6	24.0 ± 3.7	7 (28)	12 (48)	3 (12)	9 (36)	8.9 ± 7.9	0.26 ± 0.12	0.49 ± 0.32
P, Univariate analysis	.03	.37	.33	.81	.047	.21	.54	.89	.02	.94	.06
P, Multivariate analysis	.005								.004		

[a]OSI, oscillatory shear index; RRT, relative residence time; WSS, wall shear stress.

cells[11,14] that support the focal inflammatory process that is likely to underlie atherogenesis. In addition, RRT may serve as a marker of stagnant blood flow because prolongation of the RRT means the long residence time of particles near the wall. Stagnant flow prolongs residence time of atherogenic particles in the blood, thus inducing lipid exchange and recruitment of macrophages and promoting atherosclerosis. An in vivo study revealed a correlation between oscillatory or stagnant flow and vascular atherogenesis in descending aorta; in an aortic regurgitation murine model, oscillatory and stagnant flow, indicated by elevation of OSI and RRT, accelerated atherosclerotic lesion formation.[10] These results suggest that oscillatory or stagnant blood flow, which was expressed by RRT prolongation, may be one of the necessary conditions for atherosclerotic lesion formation in intracranial aneurysms.

This study poses an important question about the role of WSS in aneurysm origin. Many hemodynamic studies of intracranial aneurysms have reported that low WSS is involved in aneurysm rupture[4,7,12] and speculated that low WSS can induce degenerative vascular wall remodeling in intracranial aneurysms, which may lead to thinning or rupture of the aneurysm wall.[13] However, the results of our study raise the possibility that an aneurysm wall exposed to low WSS can progress to atherosclerotic remodeling. Although time-dependent changes of aneurysms are unknown and the following hypothesis has no determined evidences, our hypothesis is that atherosclerotic lesion formation in intracranial aneurysms may require at least 3 conditions in addition to low WSS: Endothelial cells must exist inside the aneurysm wall, which are considered to be necessary for atherosclerotic remodeling process[19,20]; there must be an interaction between vascular endothelium and blood contents because the stagnation of blood flow might play a role in providing the long residual of atherosclerotic particles in the neighborhood of the endothelium; and the aneurysm must escape from the rupture long enough to allow atherosclerotic lesion formation. We consider that low WSS is a risk for aneurysm rupture.[12] However, aneurysms with low WSS accompanied by the stagnation of blood flow may be stabilized by atherosclerotic remodeling process if they escaped from the rupture and were exposed to stagnant blood flow for enough time. Of course, the biological response under the blood flow stagnation may be modified by the inflammatory status of the host, which is modulated by atherosclerotic risks such as smoking history and metabolic disorders.

Limitations

In CFD simulations, typical simplifications are made in model generation and boundary condition settings.[21] Nonnewtonian viscosity was neglected for technical reasons in this study. The newtonian fluid assumption may underestimate the viscosity and overestimate WSS in regions of stasis.[22] Other limitations are related to wall compliance, outflow conditions, and the numerical technique used to solve the governing equations. These effects are